CHALMERS
UNIVERSITY OF TECHNOLOGY

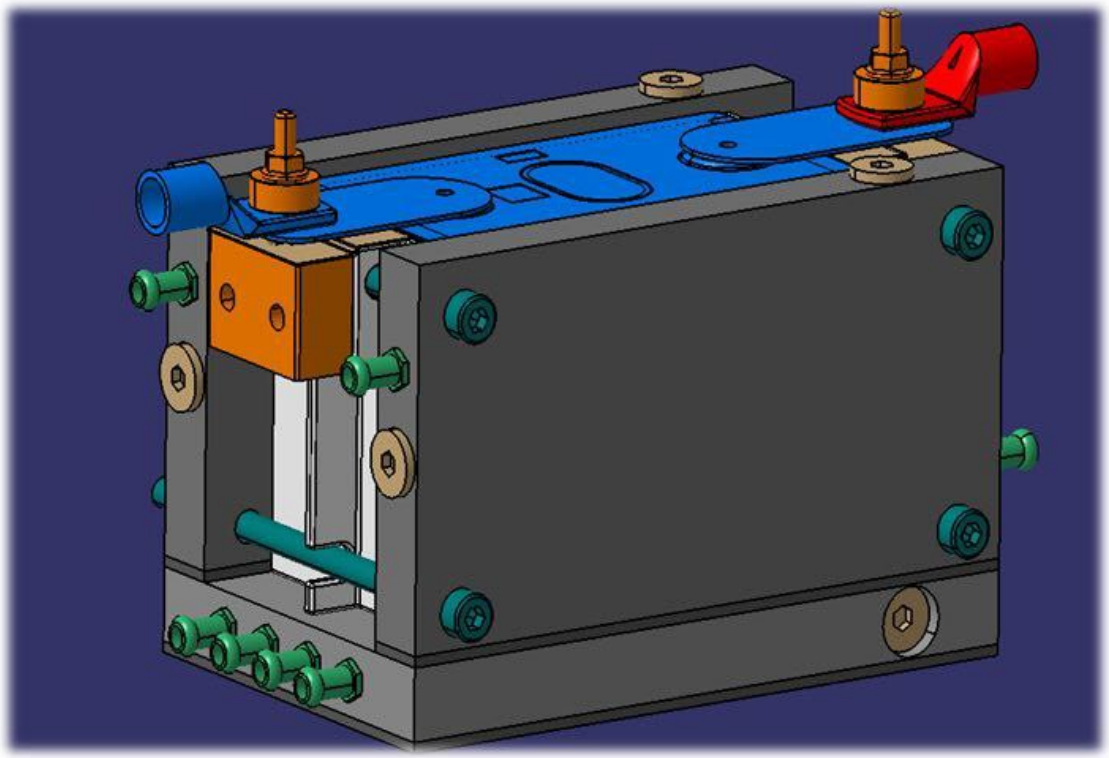

3D thermal modeling of a battery cell on a test jig fixture using CFD

Master's thesis in Sustainable Energy Systems - MPSES

REZA DANESHVARI

DEPARTMENT OF MECHANICS AND MARITIME SCIENCES

CHALMERS UNIVERSITY OF TECHNOLOGY
Gothenburg, Sweden 2023
www.chalmers.se

Master's thesis 2023

3D thermal modeling of a battery cell on a test jig fixture using CFD

Evaluation of a fast-charged battery cell thermal behavior in a test chamber, both experimentally and numerically

REZA DANESHVARI

CHALMERS
UNIVERSITY OF TECHNOLOGY

Department of Mechanics and Maritime Sciences
Division of Vehicle Engineering and Autonomous Systems
Chalmers University of Technology
Gothenburg, Sweden 2023

3D thermal modeling of a battery cell on a test jig fixture using CFD
REZA DANESHVARI

Supervisor: Ingemar Andersson, Volvo Cars Sverige
Supervisor: Maedeh Arvani, Volvo Cars Sverige
Supervisor: Anandh Ramesh Babu , Department of Mechanics and Maritime Sciences
Examiner: Prof. Simone Sebben, Department of Mechanics and Maritime Sciences

Master's Thesis 2023
Department of Mechanics and Maritime Sciences
Division of Vehicle Engineering and Autonomous Systems
Chalmers University of Technology
SE-412 96 Gothenburg
Telephone +46 31 772 1000

Cover: A simple schematic of a real jig with a battery cell installed on it before testing in a chamber.

Typeset in LaTeX
Printed by Chalmers Reproservice
Gothenburg, Sweden 2023

3D thermal modeling of a battery cell on a test jig fixture using CFD
Evaluation of a fast-charged battery cell thermal behavior in a test chamber, both experimentally and numerically

REZA DANESHVARI
Department of Mechanics and Maritime Sciences
Chalmers University of Technology

Abstract

The thermal conditioning of battery cells plays a crucial role in ensuring their safety and maximizing the driving range of electric vehicles. To gain a comprehensive understanding of battery cell performance under various conditions, testing is conducted within controlled chambers that replicate real-world scenarios. While battery packs and modules can function independently during testing, individual cells require mechanical support. This is where the jig comes into play, serving as a robust support structure that enables current conduction and facilitates effective liquid-based thermal conditioning. The objective is to achieve optimal cell climatization and maintain it at a suitable temperature.

In order to comprehend the thermal properties of the jig when exposed to the heat generated by the battery cell, Computational Fluid Dynamics (CFD) simulations are employed. These simulations provide insights into the underlying physics of the phenomena and aid in the identification of potential enhancements for the jig design or testing conditions to prevent cell damage. The model can be adjusted to simulate different temperature scenarios, allowing for a comprehensive evaluation of the jig's response under varying conditions.

Keywords: battery cell, electric vehicles, Volvo Cars, CFD, heat-transfer, thermal behavior, testing, modeling, equivalent circuit model, STAR-CCM+.

Acknowledgements

I am greatly indebted to my supervisors at Volvo Cars, Maedeh Arvani, and Ingemar Andersson, for affording me the opportunity to work on this project and for their unwavering technical support throughout my Master's thesis journey. I would also like to extend my heartfelt appreciation to Anandh Ramesh Babu, whose expertise and insightful experiences in CFD have profoundly enriched this work.
My sincere gratitude goes to Ulf Lind, Elias Samaha, and the personnel at the Volvo Cars' Battery Lab, whose warm welcome, kind assistance, and encouragement made me feel right at home. Last but not least, I would like to express my profound appreciation to my examiner, Prof. Simone Sebben, for her invaluable feedback and guidance during the thesis period. Her support and direction were deeply appreciated.

I am profoundly grateful for the support, advice, and assistance provided by all of these remarkable individuals. With their invaluable help, any remaining flaws or inadequacies in this work are solely my responsibility.

Reza Daneshvari, Gothenburg, June 2023

List of Acronyms

Below is the list of acronyms that have been used throughout this thesis listed in alphabetical order:

Ah	Amper hour
BEV	Battery Electric Vehicle
CFD	Computational Fluid Dynamics
ECM	Equivalent Circuit Model
LIB	Lithium-ion battery
OCV	Open Circuit Voltage
RCR	Resistance Capacity Resistance
SOC	State of Charge
VCC	Volvo Cars Corporations

Nomenclature

Below is the nomenclature of indices, sets, parameters, and variables that have been used throughout this thesis.

Indices

i,j,k	Dummy indices for variable or species
t	Index for turbulent variable

Greek letters

ρ	Density
ϵ	Turbulent dissipation rate
μ	Dynamic viscosity
μ_t	Turbulent dynamic viscosity
ν	Kinematic viscosity
η	Kolmogorov length scale
σ	Stefan Boltzmann constant
ϕ	Equivalence ratio
β	Coefficient of volume expansion

Parameters

C_1, C_2, C_3	k ϵ Turbulence model constants
Δt	Time discretization step (time interval)
ΔT	Temperature difference between two points in space
T_S	Surface temperature
T_∞	Ambient temperature

S_i	Source term of variable i
A	Area
P	Pressure
h	Heat transfer coefficient
g	Gravity
I	Current
R_0	Resistance
R_P	Polarization resistance
tau	Time constant
c	Current over capacity
Q	Heat generation
$q_{convevtion}$	Rate of convective heat transfer
$q_{conduction}$	Rate of conductive heat transfer

Contents

List of Figures

List of Tables

1

Introduction

1.1 Background

Vehicle manufacturers acknowledges the paramount importance of thermal conditions in determining crucial performance factors of battery technology, including its lifespan, electric vehicle driving range, power availability, and safety. To gain a comprehensive understanding of battery performance under diverse thermal conditions, it is imperative to conduct thorough testing under controlled circumstances that mimic real-world scenarios and provide valuable data [1].
Testing is carried out within enclosed chambers of varying sizes, depending on the size of the test object, which can range from a battery pack or module to a single cell. Since the battery cell, being the smallest component, lacks the ability to independently connect and support itself during testing, a mechanical support structure known as the cell jig is employed to provide both mechanical support and electrical connections to the testing equipment.

Thermal control of the battery cells is achieved through two distinct mechanisms: the ambient airflow and temperature within the cell chamber, and the liquid-based thermal conditioning system integrated within the cell jig. The liquid-based thermal conditioning system of the cell jig consists of drilled channels within the mechanical support structure and an external controller for regulating the flow and temperature of the liquid. This system enables both cooling and heating of the battery cell, depending on the setpoints defined by the liquid controller.

Given that the thermal conditioning of the battery cell on the jig occurs through the airflow within the test chamber and the liquid circulating through the drilled channels, the primary focus of this thesis project was to evaluate the thermal properties of the specific jig employed, as well as the heat distribution across the jig's surface and body when subjected to the heat generated by the battery cell. To accomplish this, heat transfer modeling using Computational Fluid Dynamics (CFD) was employed to analyze the specific areas of interest which has been used in the thesis. Furthermore, two sets of experiments was conducted simultaneously to facilitate a comparison between the simulation results and real-world observations. The data obtained from the initial experiment was utilized to refine both the CFD model and the subsequent test, minimizing deviations within an acceptable range and providing a more accurate representation of reality.

1.2 Aim

The primary objective of this master's thesis is to construct and advance a comprehensive and sophisticated thermal 3D CFD model for both the jig and the battery cell utilizing Simcenter Star-CCM+. This aim will be accomplished by conducting two sets of experiments in tandem with the mathematical model to verify its accuracy and reliability.
In addition, the following objectives were pursued:

- Building and developing a model for the empty jig that is consistent with the initial experiment.
- Enhancing the experiment's design and subsequently construct a CFD model for the jig with the battery cell mounted on it.

Through this work, we aimed to develop a highly precise and dependable thermal 3D CFD model for the jig and battery cell. By accomplishing these objectives, we anticipate identifying and addressing characteristics of present set ups and CFD model and accordingly providing invaluable insights and recommendations for future design improvements.

1.3 Limitations

The validation process for the developed model was based on experimental data; however, there are certain uncertainties surrounding the installation and accuracy of the thermocouples that may have impacted the final results.
Furthermore, due to the unavailability of the entropy table for the intended battery cell, the model for the battery cell mounted on the jig was constructed solely by implementing the equivalent circuit model. As a result, the reversible heat generation from the cell has not been taken into account.
It is also important to note that each cycle of the battery cell test took approximately one day, rendering it impossible to perform transient simulations using Star-CCM+. To address this challenge, a specific time period during the charging process was selected for comparison with experimental data.
In the final stages of the project, it became apparent that the battery cell featured a plastic cover during testing, potentially impacting the heat transfer to the jig. Additionally, the simulations did not account for contact resistance, which is a factor in determining heat transfer efficiency. Furthermore, some uncertainties were observed in the thermocouple data, with a potential variation of up $\pm$ 1 °C. These factors highlight the need for further investigation and refinement to improve the accuracy and reliability of the results.

2
Theory

The following chapter delves into the essential theoretical underpinnings that are imperative to comprehend the topics and substance presented in this report. It commences with the rudimentary principles of fluid dynamics and heat transfer pertaining to various modes, subsequently progressing to the thermal modeling of battery cells with respect to State of Charge (SOC), Resistance (R), Temperature, and other crucial parameters.

2.1 Computational Fluid Dynamics

In the field of engineering, computational fluid dynamics (CFD) is a powerful tool for simulating fluid flow, heat transfer, and chemical reactions using computer-based analysis. CFD is versatile and can be applied in a wide range of industrial and non-industrial fields. Numerical solution techniques for CFD can be broadly classified into different streams. However, for the purposes of this thesis, we will focus solely on the finite volume method. One distinguishing feature of the finite volume method is the control volume integration, which ensures the exact conservation of relevant properties for each finite size cell[2].
In CFD, the equations governing the conservation of continuity, momentum, energy, and species are solved through the application of fundamental physical laws, assuming a continuum fluid [3].

2.1.1 Continuity Equation

In computational fluid dynamics (CFD), the continuity equation is a fundamental equation that describes the conservation of mass for a fluid. It states that the rate of change of mass within a given control volume is equal to the net mass flow rate into or out of the volume. For unsteady, three-dimensional compressible and incompressible flows, the continuity equation can be expressed as follows [2]:

$$\frac{\partial \rho}{\partial t} + \nabla \cdot (\rho \vec{u}) = 0 \tag{2.1}$$

Mathematical, the continuity equation can be expressed as a partial differential equation that describes the conservation of mass in a fluid flow field. The first term of the equation describes the rate of change of the fluid density over time, while the second term represents the flux of mass in the flow field. The velocity vector u, which consists of components u, v, and w representing the flow velocities in the x, y, and z directions, respectively, is also involved in the equation.

In the case of incompressible flow, where the density of the fluid remains constant, the continuity equation can be simplified by neglecting the time derivative of density. As a result, the equation takes on a more compact form, allowing for more efficient computational implementation in numerical simulations [2]:

$$\nabla \cdot (\rho \vec{u}) = 0 \tag{2.2}$$

2.1.2 Momentum Equation

In the field of computational fluid dynamics (CFD), the momentum equation is a fundamental tool for analyzing the motion of fluids. It is derived from Newton's second law, which states that the rate of change of momentum of a fluid particle is equal to the sum of forces acting on that particle.

For unsteady, three-dimensional, and compressible flows, the momentum equations can be expressed as a set of partial differential equations that describe the velocity components in the x, y, and z directions. These equations incorporate the effects of pressure gradients, body forces, and viscous stresses on the fluid motion. It is worth noting that the momentum equation is a vector equation, and its components can be expressed in different coordinate systems, such as Cartesian, cylindrical, or spherical coordinates. In addition, the momentum equation can be simplified for certain cases, such as steady-state, two-dimensional, or incompressible flows [2]:

$$x-momentum \qquad \frac{\delta(\rho u)}{\delta t} + div(\rho\, u\, \mathfrak{u}) = -\frac{\delta P}{\delta x} + div(\mu\, grad\, u) + S_{Mx} \tag{2.3}$$

$$y-momentum \qquad \frac{\delta(\rho v)}{\delta t} + div(\rho\, v\, \mathfrak{u}) = -\frac{\delta P}{\delta y} + div(\mu\, grad\, v) + S_{My} \tag{2.4}$$

$$z-momentum \qquad \frac{\delta(\rho w)}{\delta t} + div(\rho\, w\, \mathfrak{u}) = -\frac{\delta P}{\delta z} + div(\mu\, grad\, w) + S_{Mz} \tag{2.5}$$

The first term describes how the momentum changes over time, while the second term represents the convective transport of momentum within the fluid. The third term accounts for the pressure gradient, which can drive fluid motion. The fourth term represents the diffusive transport of momentum, which is related to the viscosity of the fluid. Finally, the last term is a source term that takes into account any external forces acting on the fluid, such as gravity or centrifugal force [3].

2.1.3 Energy Equation

The energy equation is a fundamental equation in computational fluid dynamics (CFD) that describes the exchange and conversion of thermal energy in a fluid. It accounts for various physical mechanisms that contribute to heat transfer, including conduction, convection, and radiation. In addition, the equation incorporates energy sources and sinks such as chemical reactions and work done on the fluid. It is derived from the First Law of Thermodynamics and is a crucial element in fluid flow

simulations, especially those that involve heat transfer. By solving the energy equation, the temperature and other related quantities, such as heat flux and enthalpy, can be determined at various points in the fluid domain [2]:

$$\frac{\delta(\rho i)}{\delta t} + div(\rho i \mathfrak{u}) = -P\, div\, \mathfrak{u} + div(k\, grad\, T) + \Phi + S_i \tag{2.6}$$

The dissipation function represented by Φ, which characterizes the conversion of kinetic energy into thermal energy due to viscosity effects. Another important term is the temperature T, which reflects the thermal state of the fluid. Thermal conductivity k is also included in the equation, which describes how efficiently heat is transferred through the fluid. In addition to these terms, there is a source term S_i, which accounts for any internal energy sources or sinks within the fluid.

2.2 Turbulence

Turbulence in computational fluid dynamics (CFD) refers to the irregular and unpredictable behavior of fluid flow characterized by rapid fluctuations in velocity, pressure, and other fluid properties. It is a complex phenomenon that arises due to the nonlinear interactions between the fluid particles, leading to the formation of vortices and eddies of various sizes and shapes.
The turbulent flows in CFD are characterized by several fundamental features [3]:

- Irregularity: Turbulent flows are irregular, random, and chaotic, with a wide range of length scales, velocity scales, and timescales. Large eddies or vortices are the primary features of the turbulent flow, and they coexist with smaller turbulent eddies. These eddies stretch, rotate, and break up into smaller eddies as they move. The irregularity and wide range of length scales and timescales make it difficult to use a deterministic approach to turbulence simulation, and statistical models are commonly used in practical engineering simulations.
- Diffusivity: Turbulence is diffusive, which means that it allows for faster mixing rates of species, momentum, and energy than would be allowed by molecular diffusion alone. The chaotic motions in the flow facilitate turbulent diffusive transport, which occurs in all three dimensions.
- Instability: Turbulence arises due to instabilities occurring at high Reynolds numbers, when the timescale for viscous damping of a velocity fluctuation is much larger than the timescale for convective transport. The Navier-Stokes equation shows that the nonlinear convective term becomes more important at large Reynolds numbers, increasing the tendency towards instability, which is damped by viscosity. Turbulent flows appear random in time and space, and are not reproducible in detail. Even small perturbations in initial conditions, boundary conditions, and material properties can significantly affect turbulent fields, making them stochastic.
- Three-dimensionality: Turbulence is intrinsically three-dimensional. The mechanisms such as vortex stretching and vortex tilting cannot occur in two dimensions, hence turbulence is intrinsically 3D. Nevertheless, 2D simulations of turbulent flows can be performed by filtering out the 3D fluctuations and resolving the coupling between the fluctuations and the mean flow field [3].

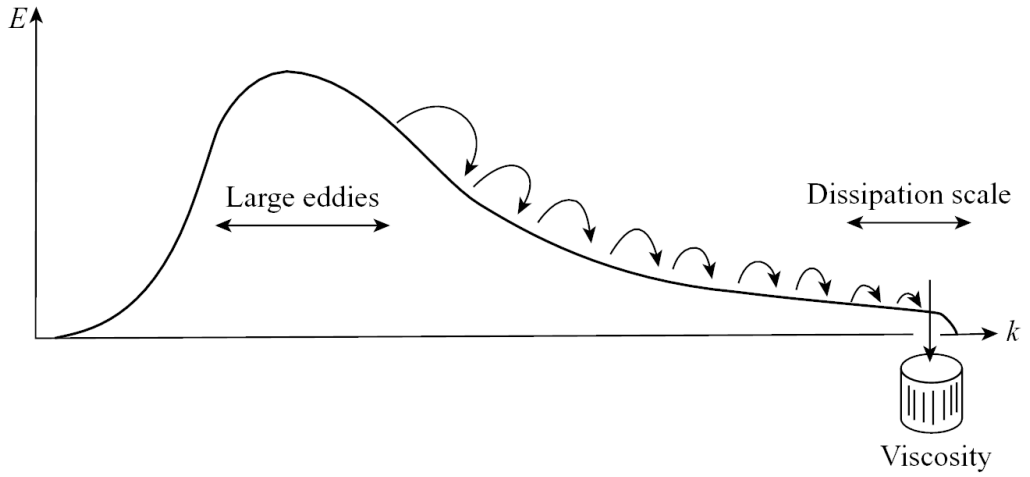

Figure 2.1: Turbulent energy cascade example, from [4]

- In all turbulent flows, there is a flux of energy from the largest turbulent scales to the small scales. The kinetic energy is transferred from large eddies to smaller eddies, which undergo similar break-up processes and transfer the energy to yet smaller eddies. Finally, the smallest eddies dissipate the turbulent kinetic energy into heat due to viscous action, which leads to the decay of turbulence if no energy is supplied to the system.
- Turbulence is a continuum phenomenon in which the properties of fluid can be considered continuous, even though the flow consists of many small eddies with a wide range of length scales. Overall, these characteristics of turbulence in CFD are essential to understanding and modeling the complex behavior of turbulent flows [3].

2.2.1 Turbulence modeling

CFD simulations make use of different turbulence models to precisely forecast fluid behavior. In this study, particular attention is given to the realizable k-epsilon model, which was employed for the simulations. Unlike the standard k-ϵ model, the realizable model includes a realizability constraint on the predicted stress tensor. Consequently, it is commonly known as the realizable k-ϵ model.

The realizable k-ϵ model and the standard k-ϵ model differ primarily in the treatment of the k equation. In the standard model, the normal stress can exhibit negative values in flows with high mean strain rates. This is problematic because the normal stress, being the sum of squares, should always be positive. However, under certain conditions, such as significant strain, the normal stress can become negative. To overcome this issue, the realizable k-ϵ model introduces a variable C, which is no longer a constant but varies based on the local flow characteristics. This adjustment ensures that the normal stresses remain positive[3].

In addition, the realizable k-ϵ model incorporates a revised epsilon equation that includes a production term accounting for turbulent energy dissipation. This adjustment distinguishes it from both the standard and RNG (Renormalization Group) k-ϵ models. While the standard k-ϵ model provides reasonable predictions for the spreading rate in planar jets, it exhibits poor performance in predicting the spreading rate of axisymmetric jets. This discrepancy can be attributed to the dissipation equation employed in the model. Conversely, the realizable k-ϵ model effectively addresses the round-jet anomaly by accurately predicting the spreading rate for both planar and axisymmetric jets.

It is worth noting that the realizable k-ϵ model is better suited for flows with high strain rates, such as those involving strong streamline curvature and rotation. Validation of complex flows, including boundary-layer flows, separated flows, and rotating shear flows, has shown that the realizable k-ϵ model performs better than the standard k-epsilon model. Overall, the realizable k-ϵ model's incorporation of the realizability constraint and its modified epsilon equation provide improved performance in predicting fluid behavior in certain types of flows. The modeled transport equations for k and ϵ in the realizable k-ϵ model are [3]:

$$\frac{\delta}{\delta t}(\rho k) + \frac{\delta}{\delta x_j}(\rho k u_j) = \frac{\delta}{\delta x_j}[(\mu + \frac{\mu_t}{\sigma_k})\frac{\delta k}{\delta x_j}] + G_k + G_b - \rho\epsilon - Y_M + S_K \tag{2.7}$$

and

$$\frac{\delta}{\delta t}(\rho\epsilon)+\frac{\delta}{\delta x_j}(\rho\epsilon u_j) = \frac{\delta}{\delta x_j}[(\mu+\frac{\mu_t}{\sigma_\epsilon})\frac{\delta\epsilon}{\delta x_j}]+\rho C_1 S_\epsilon-\rho C_2\frac{\epsilon^2}{k+\sqrt{v\epsilon}}+C_{1\epsilon}\frac{\epsilon}{k}C_{3\epsilon}G_b+S_\epsilon \tag{2.8}$$

where

$$C_1 = max[0.43, \frac{\eta}{\eta+5}], \qquad \eta = S\frac{k}{\epsilon}, \qquad S = \sqrt{2S_{ij}S_{ij}} \tag{2.9}$$

The generation of turbulence kinetic energy due to mean velocity gradients is denoted by G_K, Similarly, the generation of turbulence kinetic energy due to buoyancy is represented by G_b. The contribution of fluctuating dilatation to the overall dissipation rate in compressible turbulence is denoted by Y_M. The constants C_2 and C_1 are also used in the equations. In addition, the turbulent Prandtl numbers for k and epsilon are represented by σ_K and σ_ϵ, respectively. The user-defined source terms S_K and S_ϵ represent external sources of turbulence kinetic energy and dissipation rate, respectively.

2.3 Heat Transfer

Thermal transfer, also known as heat transfer, is the process of energy transfer between two objects that have a temperature difference. The second law of thermodynamics states that heat always flows from a hotter body to a colder body, and the direction of heat transfer is fixed. Over the years, researchers have classified heat transfer into three categories: conduction, convection, and radiation [6].

2.3.1 Conduction

Thermal conduction is the process of energy transfer from a substance's more energetic particles to its less energetic particles. It occurs due to the interactions between them. The transfer of energy through thermal conduction is important in many areas of science and engineering, such as building insulation, electronic devices, and industrial heat exchangers.
The energy contained in molecules is related to their random translational motion, as well as their rotational and vibrational motions. When molecules collide, they transfer energy to each other, resulting in an increase in temperature. Higher temperatures are directly related to higher molecular energies, so the particles in a material located closer to a heat source will contain more energy than the particles located further away. This creates a temperature gradient through the material, with temperature decreasing as distance from the heat source increases.
As a simple example, consider a car door with heated air inside and colder air outside. The temperature gradient through the door means that the particles in the door closer to the heated air will contain more energy than those closer to the colder air. As the higher-energy particles collide with the lower-energy particles, they transfer some of their energy. This process of energy transfer continues throughout the door, resulting in a net transfer of energy from the hotter side of the door to the colder side.
Conductive heat transfer can occur in solids, liquids, and gases, with the main difference between them being the spacing of the molecules within the medium. In solids, the molecules are tightly packed, so energy transfer through thermal conduction is generally more efficient than in liquids or gases. However, the efficiency of energy transfer through thermal conduction can be affected by various factors, such as the thermal conductivity of the material, its shape and size, and the presence of thermal insulation.
To quantify the rate of heat transfer through thermal conduction, Fourier's law can be used. This equation provides a mathematical expression for the amount of energy transferred per unit time. In one dimension, Fourier's law is expressed as follows:

$$q''_x = -kA\frac{dT}{dx} \tag{2.10}$$

where q is the heat flux, k is the thermal conductivity of the material, A is the cross-sectional area, T is the temperature, and x is the distance through the material. This equation demonstrates that the rate of energy transfer through thermal conduction is directly proportional to the temperature gradient and the cross-sectional area, and inversely proportional to the distance between the two points and the thermal conductivity of the material [6].

2.3.2 Convection

Convection is the process of heat transfer by the movement of a fluid. This occurs because the molecules in the fluid are in constant motion, and the hotter molecules have more kinetic energy. As a result, the hotter molecules transfer their energy to the colder molecules, causing the fluid to flow and the heat to be transferred.

There are two main types of convection: natural convection and forced convection. Natural convection occurs when there is a temperature gradient in an enclosed volume, which causes the fluid to flow due to buoyancy effects. Forced convection, on the other hand, occurs when an external force, such as a fan or a pump, is used to move the fluid.
In this project, we were concerned with both convections. When a heat source is placed in an enclosed volume that is not a vacuum, the temperature gradient that is established in the volume causes the air to heat up and expand. This expansion causes the density of the air to decrease, which leads to the displacement of the air molecules due to the effect of buoyancy. This induced motion participates in heat transfer and is important to consider during the modeling process.
According to Newton's law of cooling, the rate of convective heat loss is proportional to the difference in temperature between the surface and the ambient temperature to which it is losing heat. The convective heat transfer rate is given by the equation

$$q_{convection} = hA(T_S - T_\infty) \tag{2.11}$$

where $q_{convection}$ is the rate of convective heat transfer, h is the convective heat transfer coefficient, A is the area of the surface exposed to heat transfer by convection, T_S is the temperature of the surface, and T_∞ is the ambient temperature.
In the thesis, the commercial Computational Fluid Dynamics (CFD) tool, Star-CCM+, was utilized to simulate natural and forced convection. Star-CCM+ offers various approaches for modeling natural convection. These include the Boussinesq approximation, incompressible ideal gas, and compressible ideal gas methods. The choice of approach depends on the specific characteristics of the problem at hand. For this master's thesis, the incompressible ideal gas approach was selected as the most suitable. This method involves the software computing fluid properties, based on the ideal gas assumption.[5].

2.3.3 Radiation

Thermal radiation is the final mode of heat transfer. It involves the emission of energy by matter at a temperature greater than absolute zero. This energy takes the form of electromagnetic waves, which can be transferred through a vacuum or a medium. The rate at which energy is emitted by a surface is called its emissive power, E, and is expressed in $\frac{W}{m^2}$. In the case of an ideal radiator, also known as a blackbody, emissive power can be calculated using the Stefan-Boltzmann law:

$$E_b = \sigma T_S^4 \tag{2.12}$$

where E_b is the emissive power of a blackbody,T_S is the surface temperature of the matter, and σ is the Stefan-Boltzmann constant (σ=5.67 $\times 10^{-8} W/(m^2.K^4)$.

However, most surfaces are not perfect radiators and their emissive power is determined by a material property called emissivity (ϵ), which ranges from 0 to 1 and describes how efficiently a surface can emit energy relative to a blackbody.

$$E = \epsilon \sigma T_S^4 \tag{2.13}$$

In addition to radiation from a surface, radiation can also be received by a surface from its surroundings. This energy, known as irradiation (G), increases the thermal energy of the surface by being absorbed by the material. The amount of energy absorbed by the material is determined by a material property called absorptivity (α). Similar to the other modes of heat transfer, the net rate of radiation heat transfer per unit area can be calculated using the following equation

$$q''_{rad} = \frac{q}{A} = \epsilon E_b T_s - \alpha G = \epsilon\sigma(T_S^4 - T_{surrounding}^4) \tag{2.14}$$

In this equation, the net rate of radiation heat transfer per unit area is determined by the difference between the thermal energy emitted and the thermal energy absorbed by the surface [5].

It is important to emphasize that radiation was not considered in this thesis study. The focus was on examining small temperature variations where the influence of radiation is minimal.

2.4 Battery Heat Generation

In the context of lithium-ion batteries, the generation of heat is a complex process influenced by various electrochemical reactions and electrical-thermal conversions. During normal battery operation, heat is produced through reversible electrochemical reactions, irreversible Joule heating, secondary reactions, and mixing processes. However, in high-power batteries, the heat generated from secondary reactions and mixing is typically negligible and can be ignored. Therefore, under this assumption, changes in temperature and state of charge (SOC) are primarily considered to be spatial in nature [7].
A simplified heat generation model that can describe the heat generation process inside the battery is:

$$Q = I^2 R(I, SOC) - IT\frac{\delta E(SOC)}{\delta T} \tag{2.15}$$

where Q represents the heat generation rate, I represents the charge or discharge current (A), which is negative in the charge process and positive in the discharge process. R represents the direct current (DC) resistance in the battery, T represents the battery temperature, E represents the open-circuit potential. Based on Eq. 2.15, it is evident that the battery heat generation rate is a function of ambient temperature, charge/discharge rates, and resistance.

The generation of irreversible Joule heat in batteries is primarily determined by the varying direct current (DC) resistance, which is not a fixed value. The DC resistance comprises ohmic resistance and polarization resistance. The ohmic resistance follows Ohm's law and depends on the battery's material properties and geometric structure, independent of the state of charge (SOC). On the other hand, polarization resistance arises from the polarization between the positive and negative electrodes during electrochemical reactions. Its magnitude is affected by the SOC and increases

with higher current densities [7].

During high charge/discharge rates, the dominant factor in heat generation is typically the irreversible Joule heat, while the reversible heat, known as entropy change in electrochemistry, is relatively small in comparison. Consequently, the reversible heat is often considered negligible, and the focus is on the irreversible Joule heat as the primary heat generation mechanism. However, relying solely on this approach can lead to deviations from the actual value. Additionally, to accurately measure terminal voltage variations under transient conditions, careful selection of data within a suitable time interval is necessary, as the choice of time interval can introduce errors. Therefore, this method may not always provide accurate results[7].

It is important to acknowledge that while this approach may not be the most optimal or accurate one, it was chosen for the purpose of this thesis project due to its affordability. Accessible electrochemical models, which offer greater accuracy for cell modeling, tend to be more expensive when coupled with CFD simulations considering the allotted simulation time and the need for a robust model setup.

3

Methods

This section provides an in-depth analysis of the methodologies utilized and advanced for the execution of the experiment and the construction of the computational fluid dynamics (CFD) model in a systematic manner. The purpose of this section is to present a clear picture of the techniques employed to ensure the accuracy and precision of the experimental results and the CFD model.

The first part of this section provides an overview of the chambers and their applications in the battery laboratory for different commercial and testing purposes. The detailed description of the chambers includes their features, capabilities, and limitations. The next part of this section focuses on the jig, which is an essential component of the experimental setup. The jig is described in detail, including its different building blocks and the installation process during the test in a chamber. Finally, the section explains the project's approach to achieving comparable data and results for both the experiment and the CFD model. The procedures used to ensure the accuracy and validity of the results are discussed in detail.

3.1 Chambers

The advancements in battery technology have enabled the development of smaller and more energy-dense batteries. However, it is imperative for companies implementing these technologies to ensure the safety of their advanced products in the market. As the energy density of battery cells increases, so does the risk of fire or explosion, potentially leading to dangerous accidents for consumers. The most well-known of these accidents is thermal runaway, a phenomenon in which battery cells spontaneously ignite. Therefore, it is crucial for companies to take measures to mitigate the risks associated with battery technology, especially when implementing advanced and energy-dense products in the market [8].
To ensure that the battery products are safe for consumers, failures due to design flaws or internal chemistry of battery cells should be identified and estimated through controlled testing conditions that mimic real-world consumer environments, prior to the release of the products into the market. Chambers are the ideal devices to create such conditions, enabling the simulation of ambient air, charging, and commercial coolant thermal conditioning, which can both cool down or heat up the battery components.

3.1.1 Types of chambers

In order to test battery components at various scales, Volvo Cars has implemented chambers of varying sizes, ranging from the largest one capable of testing an entire battery pack to the smallest one designed for battery cell testing. Despite their size differences, these chambers serve the same purpose. It should be noted that the older chambers have limited capabilities compared to the newer ones, which may include humidity control, but this is not within the scope of this thesis. The chambers are operated by skilled test engineers who monitors and reports any hazardous risks, such as fire, explosion, or toxic gases. The test engineers also collects and analyzes data during testing, including thermocouple temperature, coolant temperature, and current rate.

Figure 3.1: An example of a chamber for the cell [12]

In this thesis study, the experimental procedure involved inserting both the empty jig and the jig with the cell mounted onto it inside the chamber. The current was then routed through the cell via busbars, while a specialized hose was utilized to deliver the liquid into the jig. It should be noted that the chamber was capable of accommodating three different jigs simultaneously and conducting the tests under the same ambient and coolant temperature but with varying currents. An image depicting the actual jig and chamber is presented below:

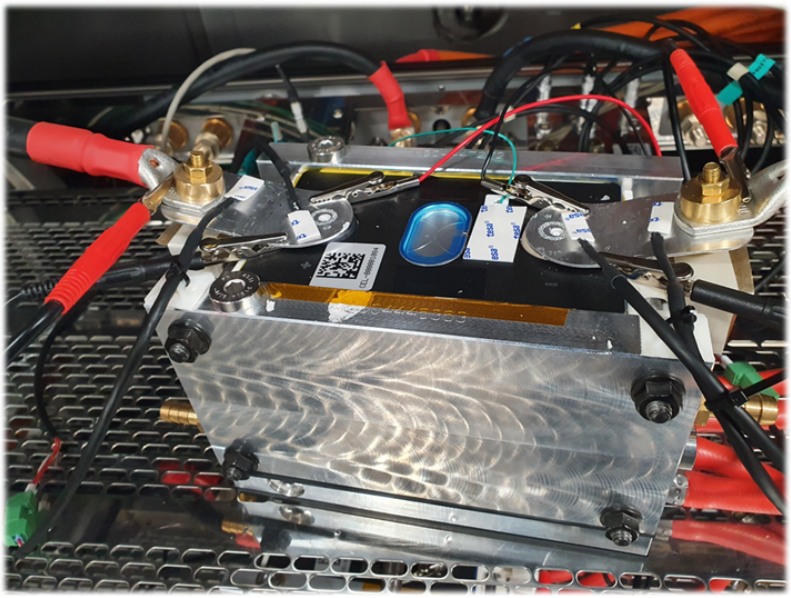

Figure 3.2: A battery cell affixed to a jig inside the test chamber before testing

3.2 Description of the jig

In the experimental setup of this thesis, the jig comprises three distinct aluminum plates with specific functions. As depicted in Figure 3.3, the image displays a jig which is used for holding the battery cell during testing:

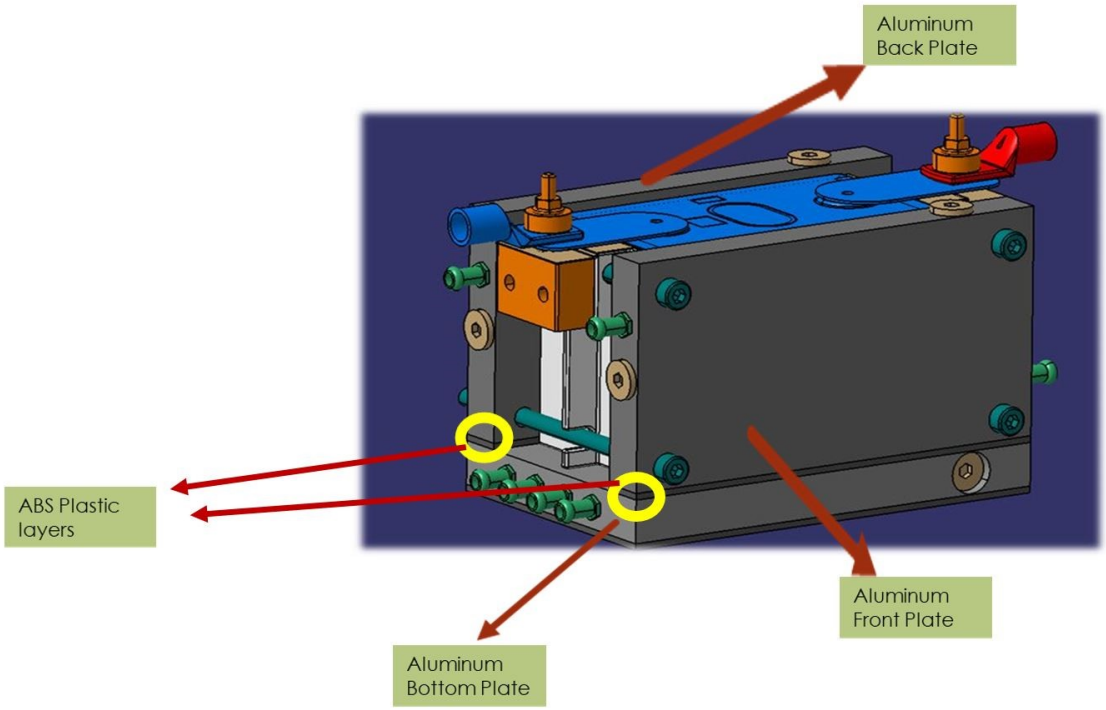

Figure 3.3: An illustration showcasing various components involved in the fabrication of the jig

As depicted in Figure 3.3, the jig is comprised of three aluminum plates, with two thin ABS plastic plates used to attach the vertical plates to the bottom plate to form a complete fixture. Figure 3.4 illustrates that the bottom plate has two separate channels, and each vertical plate contains a single channel through which the coolant flows. It is important to note that the jig was constructed in a manner such that the outlet of each bottom channel is linked to the vertical ones. This implies that the coolant from the chamber first enters the jig through the bottom plate, and then a single hose is employed to connect the outlet coolant of the bottom plate to the vertical plate. As a result, when we refer to the outlet temperature from the jig, we are referring to the temperature of the vertical plates' outlet, which means number 5&6 in the Figure 3.4.

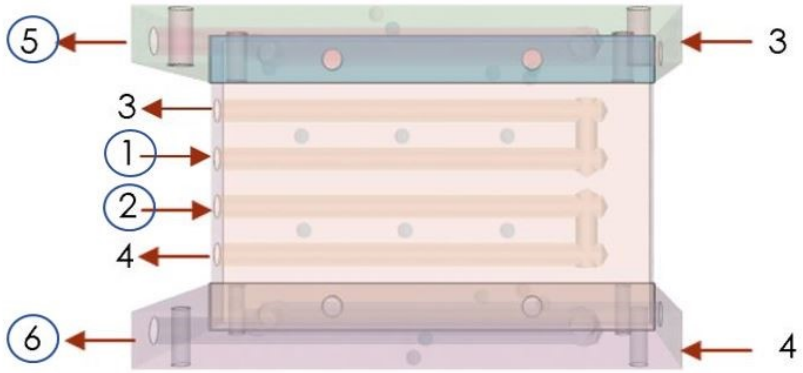

Figure 3.4: An illustration depicting the entry and exit points of the jig

3.3 Experiments

Two sets of experiments were meticulously planned and executed on separate weeks. The purpose of these experiments conducted within the chamber was to ensure that the methodology and data obtained would be comparable to the results obtained from a 3D simulation. This approach aimed to enhance our understanding of the research presented in this thesis and achieve the desired objectives.

3.3.1 Experiment 1

The first experiment was divided into two distinct parts. Initially, the empty jig was subjected to testing inside the chamber under extreme conditions, where a significant temperature difference existed between the ambient temperature and the coolant temperature. This approach was chosen for several reasons:

i. No heat source was introduced in this initial test.

ii. No adhesive tapes were used (a comprehensive explanation of adhesive tapes and their functions is provided in Section 3.3.2.2.)

iii. An agreement was made in advance to first establish a reliable model for the empty jig itself before incorporating the battery model into it.

A total of 18 thermocouples were strategically placed at various locations on the empty jig, and also including some more inside the hose to monitor the temperature and mass flow rates of the coolant entering and exiting the chamber.The figure 3.5 illustrates the arrangement of thermocouples on the bottom plate as an example, each identified by a unique number.

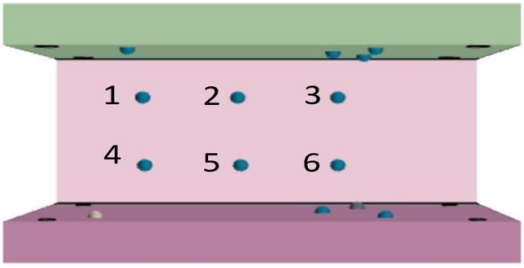

Figure 3.5: The placement of the thermocouples on the bottom plate

For the second portion of the first experiment, a battery cell mounted on a separate jig with similar properties was utilized to investigate the data obtained when a heat source was present. Notably, when the battery cell was introduced, the experimental conditions were adjusted to ensure both the coolant and ambient temperatures were maintained at a safe 35°C, following recommended operating conditions for battery cell testing from Battery Lab's test engineers.

3.3.2 Experiment 2

In the second experiment, the entire procedure from the first experiment was repeated, with the only difference being the use of adhesive tapes on top of the thermocouples. This modification aimed to provide an additional layer of isolation from the ambient air, further refining the experimental setup. Here an example of an empty jig with thermocouples installed on it is shown in the Figure 3.6.

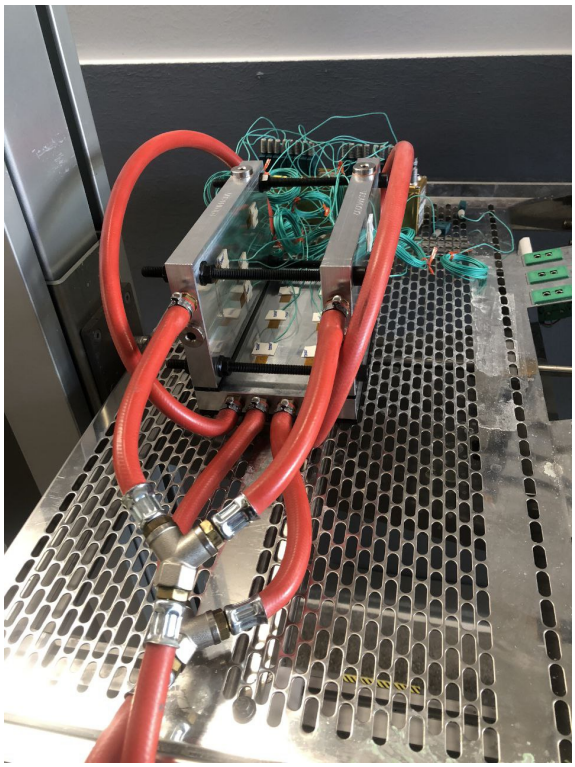

Figure 3.6: An empty jig with thermocouples installed on it, ready for the test

3.3.2.1 The hot wire anemometer sensor

The hot wire anemometer sensor is a device used to measure air velocity or flow rate in various applications. It operates on the principle of convective heat transfer and relies on a thin, heated wire as the sensing element. It consists of a wire made of a material with high electrical resistance, such as platinum or tungsten. This wire is typically very thin and has a length of a few millimeters. It is mounted within a probe or sensor housing, which is designed to be inserted into the airflow being measured. When an electric current passes through the wire, it heats up due to its electrical resistance. The wire acts as a small heated element within the airflow. As the airflow passes over the wire, it carries away heat from the wire, causing its temperature to decrease. The rate of heat loss is directly related to the velocity of the airflow [13].
The hot wire anemometer operates based on the principle of convective heat transfer. As the airflow velocity increases, the convective heat transfer coefficient also increases, leading to a greater rate of heat loss from the wire. This change in heat loss corresponds to the change in airflow velocity, allowing the sensor to provide accurate velocity measurements [13].

Figure 3.7: An example of a hot wire anemometer [14]

3.3.2.2 Adhesive tapes

Adhesive tapes are versatile materials commonly used in various industries and applications due to their unique properties and functions. These tapes consist of a foam substrate coated with a pressure-sensitive adhesive on one or both sides. The foam substrate is typically made from materials such as polyethylene, polyurethane, or PVC, which provide flexibility, cushioning, and excellent conformability.
One of the primary functions of adhesive foam tapes is to provide bonding and sealing capabilities. The adhesive layer on the tape adheres firmly to different surfaces, creating a strong and durable bond. This feature allows for secure attachment of materials, such as joining two components together or mounting objects onto surfaces. The foam substrate helps distribute the stress and load evenly, reducing the risk of failure or detachment.Another important function of adhesive foam tapes is vibration damping. The compressible foam absorbs and dissipates vibrations, reducing noise and minimizing the transmission of shocks or vibrations between components [9].

In order to assess the efficacy of thermocouples in measuring temperature, both with and without the use of adhesive tapes, the initial set of experiments deliberately omitted the application of these tapes.

Figure 3.8: A common commercial adhesive tape [10]

3.4 Computational Fluid Dynamics

3.4.1 Natural convection

For the Computational Fluid Dynamics (CFD) simulations, the Computer-Aided Design (CAD) file of the empty jig was obtained and underwent some necessary modifications, including the removal of extraneous components such as screws and bars. This was done because these components were deemed to have minimal impact on the expected results, considering their properties and functions within the fixture, and their inclusion would only add unnecessary complexity and cost to the simulations.

Upon the arrangement of the geometric components, it became apparent that the functioning of the chamber in achieving the desired ambient temperature was uncertain. As a result, a deliberate choice was made to exclusively focus on natural convection for the heat transfer of the aluminum plates, without considering any airflow. This decision aimed to facilitate the calculation of natural convection heat transfer by Star-CCM+. To enable this, the heat transfer coefficient (HTC) for each plate was calculated using empirical equations.

Initially, the Grashof Number, which quantifies the balance between buoyancy and viscous forces exerted on the fluid element, was computed to assess the occurrence of free convection:

$$Gr = \frac{g\beta(\delta t)L^3}{\nu^2} \tag{3.1}$$

Where g is the acceleration due to gravity (m/s^2), β is the coefficient of volume expansion, δt is the temperature difference between the coolant and the ambient, ν is the kinematic viscosity ($\frac{\mu}{\rho}$) (m^2/S), and L is the characteristic length (m). β

could be obtain as:

$$\beta = \frac{1}{T_{ref}}$$

$$T_{ref} = \frac{T_{coolant} + T_{ambient}}{2}$$

Subsequently, the Rayleigh number, employed to determine the laminar or turbulent nature of natural convection, was computed. This parameter is obtained by multiplying the Grashof number with the Prandtl number. The Rayleigh number is closely associated with the Nusselt number and signifies the interplay between buoyancy forces and the stabilizing influence of viscous forces:

$$Ra = Gr \times Pr \tag{3.2}$$

Prandtl number of the air is usually considered to b e 0.71. For the most industrial cases if Ra<10^9, the fluid is laminar and if Ra>10^9, it is turbulent. For this thesis case, the fluid was calculated to be laminar.
Then, the Nusselt number, another dimensionless parameter, was obtained. This number is used to determine the ratio of convective heat transfer to conductive heat transfer:

$$Nu = \frac{hL}{k} = C \times Ra^n \tag{3.3}$$

Where C and n are constant values equal to 0.59 and $\frac{1}{4}$ [11]. By knowing the the Nu number, the heat transfer coefficient (h) could be obtained for each plate and imported inside the Star-CCM+ as a one of our boundary conditions.
In the subsequent stage, the determination of the coolant flow's laminar or turbulent nature was accomplished by calculating the Reynolds number using the following formula:

$$Re = \frac{\rho U L}{\mu} \tag{3.4}$$

Where ρ is the density in $\frac{Kg}{m^3}$, U is the velocity of the fluid (m/S), L is the characteristic length (m) and μ is the dynamic viscosity ($\frac{N.s}{m^2}$). For the pipe flow:

$$\begin{cases} Laminar, & Re \leq 2300 \\ Transitional & 2300 \leq Re \leq 2900 \\ Turbulent, & Re \geq 2900 \end{cases} \tag{3.5}$$

In the context of this thesis, it was determined that the coolant flow from the chamber into the jig exhibited laminar characteristics as the Reynolds number was around 870, thus eliminating the need for turbulence modeling in this particular aspect.

After configuring the remaining boundary conditions, such as the ambient and coolant temperature, as well as the coolant flow rate, a thorough mesh study was conducted. Given that it was a conjugate heat transfer simulation, the user guide within Star-CCM+ recommended employing a conformal mesh. To ensure that our solution achieved mesh independence, we decided to monitor the variation in coolant outlet temperature for different cell sizes. This approach was motivated by the fact that the sensor installed inside the hose was provided by the chamber manufacturer,

not the battery lab technician, and it remained in place throughout the experiment sets. By doing so, we could obtain more reliable and trustworthy results. Subsequently, the target mesh was selected when the outlet coolant temperature from the jig exhibited a deviation of no more than 0.1 degrees, thereby satisfying our desired level of accuracy.

Mesh	Number of cells	Coolant outlet temperature (°C)
Coarse	601589	59.2
Optimum	1076109	59.47
Fine	1750972	59.43
Very fine	1874593	59.43

Table 3.1: Mesh size study results displayed in a table

The optimum mesh from Table 3.1 has around 1076109 number of cells. We decided to move forward with the work with optimum case and build the rest part of the simulation based on that. For this mesh, the wall y^+ was below 1.

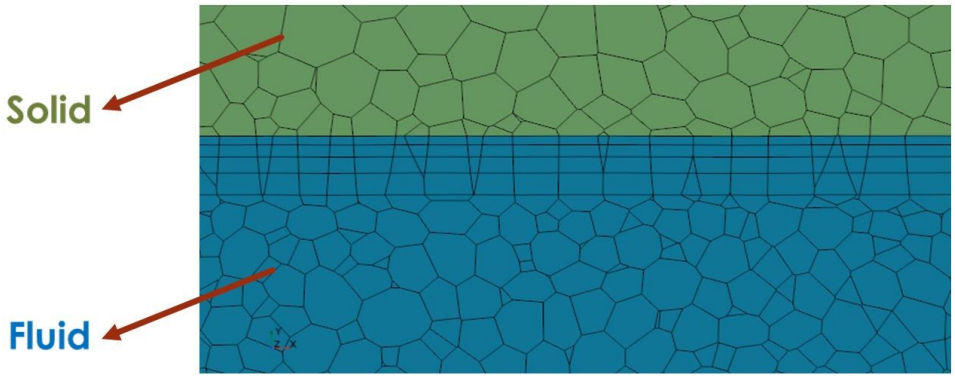

Figure 3.9: A representation of the conformal mesh

3.4.2 Forced convection

To investigate the occurrence of forced convection and to gain a deeper insight into the air circulation dynamics inside the chamber, a comprehensive analysis was conducted by measuring the air flow at 12 distinct locations using a hot wire anemometer sensor. This approach aimed to enhance our understanding of the intricate airflow patterns and provide valuable insights for further refinement of the simulation model (See 3.3.2.1).
In order to conduct the measurement, the hot wire anemometer sensor was manually positioned at 12 distinct locations within the chamber enclosure. After analysis of the sensor data revealed a consistent pattern: the airflow originated from the lower section of the chamber and ascended towards a fan, which functioned to extract the air. Consequently, the highest air velocities were observed near the bottom of the

chamber.

To simulate this scenario within the Star-CCM+, a computational domain was constructed resembling the chamber surrounding the jig, accurately representing its position within the chamber. To define the inlet velocity for the air flow, the average velocity of the three closest points to the chamber inlet was taken into consideration. The air was modeled as an ideal gas, accounting for factors such as gravity, buoyancy, and hydrostatic pressure. Considering the turbulent nature of the flow, the realizable $k - \epsilon$ turbulence model was selected as the most appropriate choice. This increased the number of the computational cells into around 2.8 million cells.

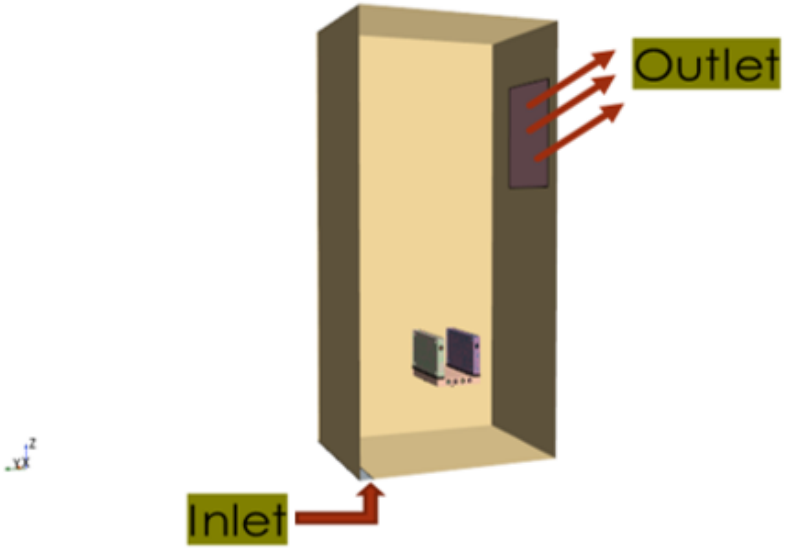

Figure 3.10: A representation of the air region inside Star-CCM+

3.4.3 Battery cell modeling inside the CFD domain

After conducting comprehensive experiments and validating the jig model inside the chamber, the focus shifted towards modeling the battery cell for rest part of the work. In order to incorporate the heat generation properties of the battery cell into the CFD modeling process, it was necessary to utilize the equivalent circuit model (ECM).

The ECM model comprises a 2D table that establishes the relationship between the resistance of the battery cell and its state of charge (SOC) and temperature. At the outset, discrete data points are obtained through experimental measurements or numerical simulations to capture the electrical behavior of the battery cell. These data points connect the cell's state variables, such as voltage, current, temperature, and state of charge [15]. The key constituents of the ECM are depicted in the figure below, showcasing its main elements.

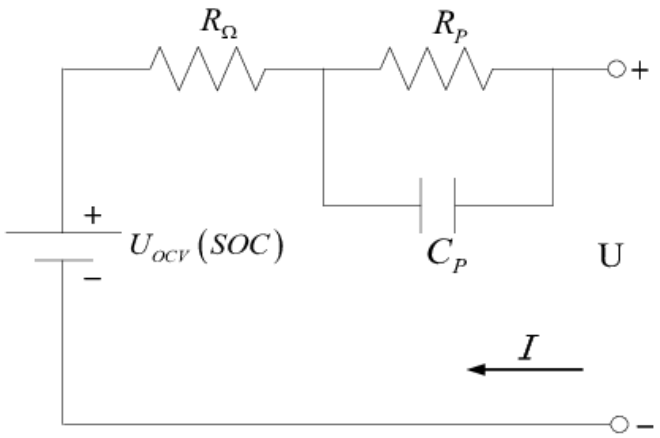

Figure 3.11: An illustrative representation showcasing ECM parameters for a battery cell [16]

The battery cell's State of Charge (SOC) indicates its level of charge, while the Open Circuit Voltage (OCV) represents the voltage across the cell's terminals without any external load or charging/discharging. The OCV is the equilibrium voltage of the cell, which is affected by factors such as SOC and temperature. [17].

The symbol R_0 represents the ohmic resistance, which characterizes the internal resistance of the battery cell's components and electrolyte. It quantifies the resistance encountered by the current flow inside the cell. [18]. The polarization resistance (R_P) characterizes the resistance associated with electrochemical reactions occurring at the electrodes of the battery cell. It encompasses various non-linear effects, including electrode kinetics and ion transport processes, contributing to the overall resistance of the cell. [19].

The battery cell's capacity to store and release electrical energy is represented by the parameter C_P, known as capacitance. It reflects the cell's ability to store electrical energy. Furthermore, the time constant, denoted by "tau," plays a crucial role in describing the cell's electrical behavior. It signifies the rate at which the cell reacts to variations in voltage and current. The ECM table includes a parameter called tau that plays a crucial role in understanding the voltage behavior during charging and discharging of the battery cell. Tau represents the time it takes for the voltage to reach 63.2% of its final value after a sudden change in current or SOC. It is determined by the product of RP (polarization resistance) and C (capacitance) as specified in the ECM model [20].

After configuring the User-Defined Battery Cell model and importing the necessary tables, a module was developed within the Star-CCM+ software to facilitate the passage of current through the cell. Additionally, a current-versus-time table based on experimental data for a half cycle was imported. This table represented the current profile during the fast-charging mode, starting from 0 amperes and increasing to a high value in a short period of time.

In order to accurately capture the behavior of the battery cell and seamlessly integrate the data, the Bezier interpolation method was utilized. This technique calculates intermediate values based on resistance points, resulting in a continuous mathematical model. By employing this approach, precise predictions of the battery cell's performance can be made across different operating conditions within Simcenter Star-CCM+.

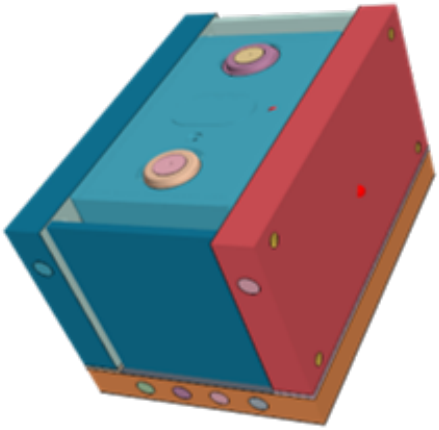

Figure 3.12: Illustration depicting the battery cell and accompanying jig configuration inside the simulation domain

4

Results

This section presents the outcomes of the employed methodology in this study, encompassing both experimental and simulation findings. To ensure the confidentiality of the battery cell and chamber data, certain measures have been taken, such as data normalization and strategic graph presentations, to effectively convey the key points while safeguarding sensitive information.

4.1 Experiment 1 and CFD

In this section, we present the results of the preliminary experiment and computational fluid dynamics (CFD) analysis performed on the empty jig, as detailed in Chapters 3.3 and 3.4.1 only for the natural convection. We will focus primarily on discussing the outlet temperature of the coolant from the chamber, as it is considered a more reliable parameter for analysis.

Position	Experiment 1	CFD
Inlet temperature of chamber (°C)	59.7	60
Outlet temperature of chamber (°C)	54.7	59.4

Table 4.1: Comparison of Outlet Temperature between Experiment 1 and CFD 1 with Natural Convection Assumption

Based on the findings presented in Table 4.1, a significant disparity was observed between the computational fluid dynamics (CFD) and experimental results for the opulet temperature from the chamber. This disparity indicates the existence of air flow within the chamber, resulting in forced convection between the aluminum plates and the surrounding air.

In order to address this discrepancy, a simulation domain was created, incorporating a box with dimensions matching the chamber size. This box represented the air continuum within the simulation. Subsequently, three different air velocities were applied at the chamber inlet, allowing for a comparative analysis of the data obtained from the computational fluid dynamics (CFD) and the simulation. The objective was to achieve improved results in terms of the outlet coolant temperature from the chamber, as presented in the table 4.3.

Air speed (m/s)	Outlet temperature of chamber (°C)
0.5	56.5
1	55.4
2	53.9

Table 4.2: Comparison of Outlet Temperature between three different air velocities

Since the air flow with a velocity of 1 m/s closely matched the experimental results for the coolant outlet temperature from the jig, as indicated in Table 4.3, this velocity was selected as the boundary condition for comparing other data, including the temperature measurements from thermocouples installed on the jig for both the experiment and CFD. For ease of understanding, the temperatures of each plate in the jig have been compared using separate graphs and scenes, as presented below.

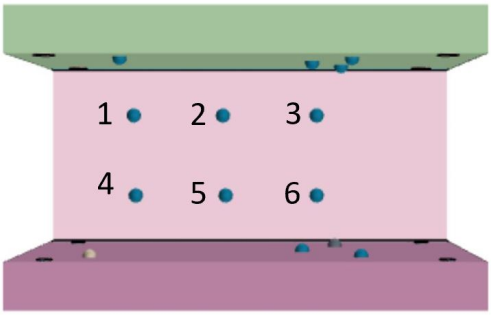

(a) Thermocouple placement on the bottom plate from a top view

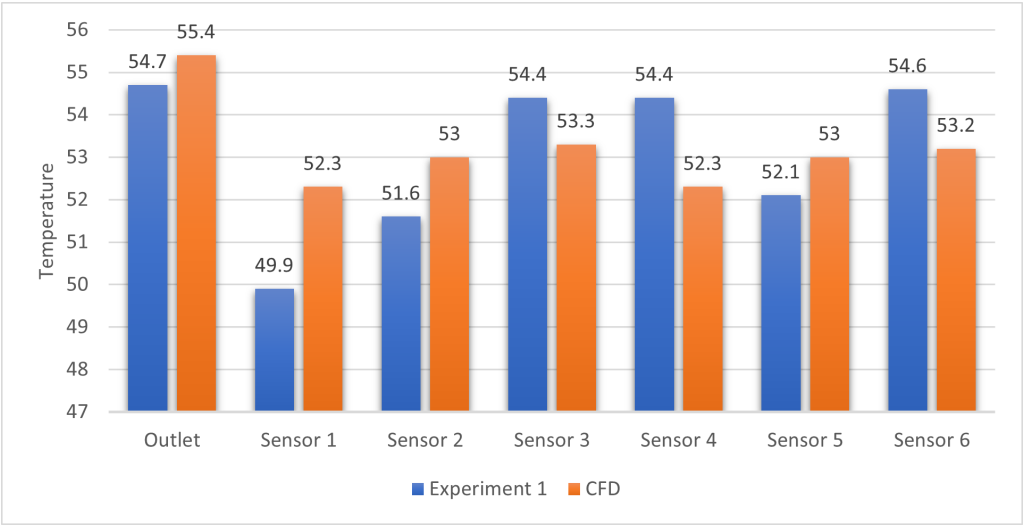

(b) Temperature of the thermocouples, from CFD and the first experiment

Figure 4.1: Comparison of the data for the air velocity of 1 m/s, for the bottom plate

The same comparisons for the back plate of the jig:

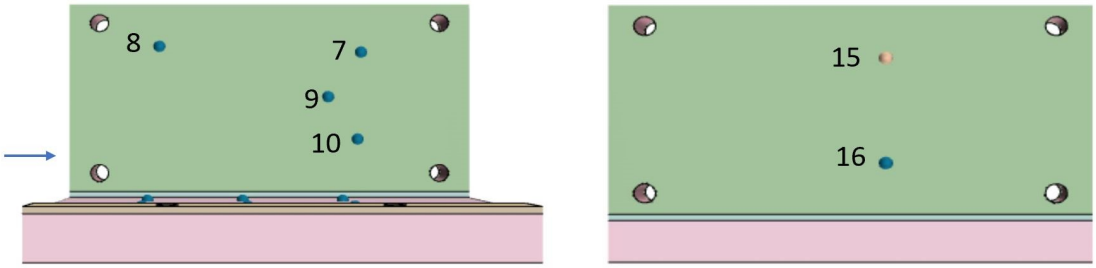

(a) Side view showing thermocouple positions on the back plate:
inner surface, outer surface (from left to right), with an arrow indicating the inlet hole

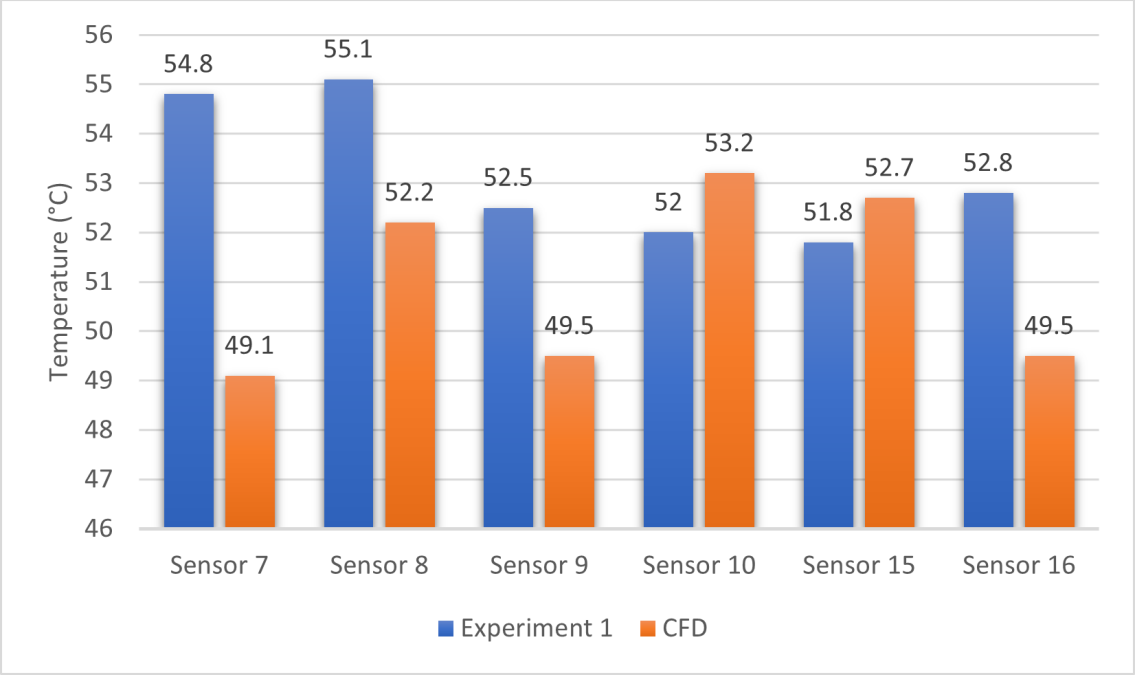

(b) Temperature of the thermocouples, from CFD and the first experiment for the back plate

Figure 4.2: Comparison of the data for the air velocity of 1 m/s, for the back plate

And, finally for the front plate:

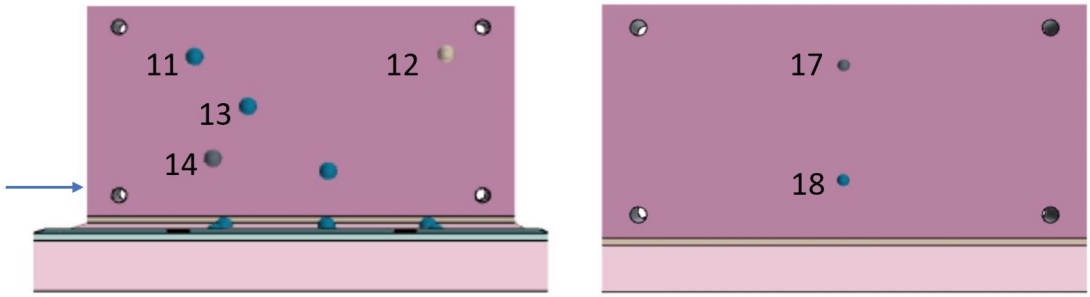

(a) Side view showing thermocouple positions on the front plate:
inner surface, outer surface (from left to right), with an arrow indicating the inlet hole

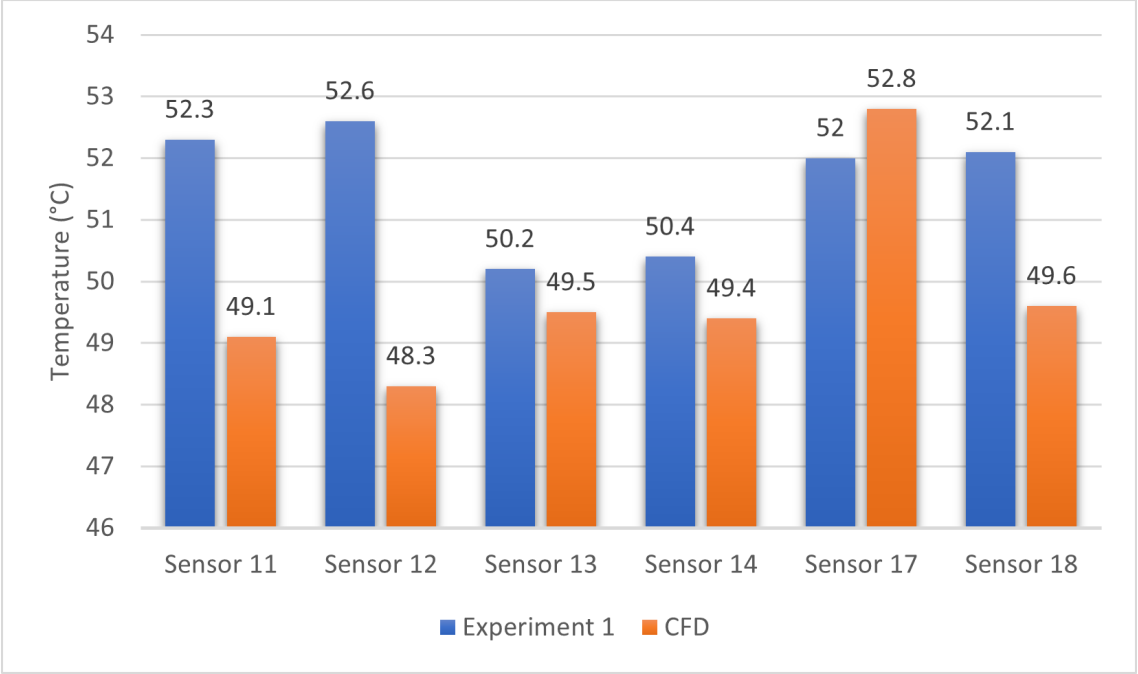

(b) Temperature of the thermocouples, from CFD and the first experiment for the front plate

Figure 4.3: Comparison of the data for the air velocity of 1 m/s, for the front plate

4.2 Experiment 2 and CFD

After conducting a comprehensive analysis and comparing the results obtained from the simulation and the experiment, certain disparities that deviated from the expected ideal scenario were observed. In order to address these discrepancies and ensure the accuracy of the experimental data, several measures were implemented.

Firstly, during the second week of the experiment, double adhesive tapes were strategically applied to the top of the thermocouples. This step aimed to enhance insulation and minimize the influence of the surrounding air on the temperature readings obtained from the jig's surface. The purpose was to evaluate the performance of the thermocouples both with and without the tapes, ensuring that the recorded temperatures aligned closely with the experiment.

Secondly, adjustments were made to the dimensions of the box representing the air continuum within the chamber. The size of the box was meticulously matched to that of the actual chamber, with the inlet positioned at the bottom and the outlet located on the top side wall. Additionally, the placement of the jig inside the chamber was carefully monitored to accurately capture its exposure to the airflow.

Thirdly, as specified in the methodology, air velocity was measured at twelve different locations within the chamber. The average velocity of the three points nearest to the chamber inlet was selected as the representative average inlet velocity for our computational domain. Here, we present the results obtained for three different plates.

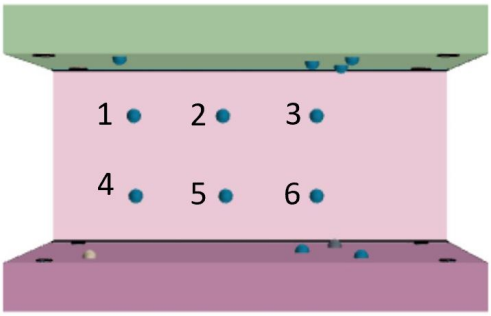

(a) Thermocouple placement on the bottom plate from a top view

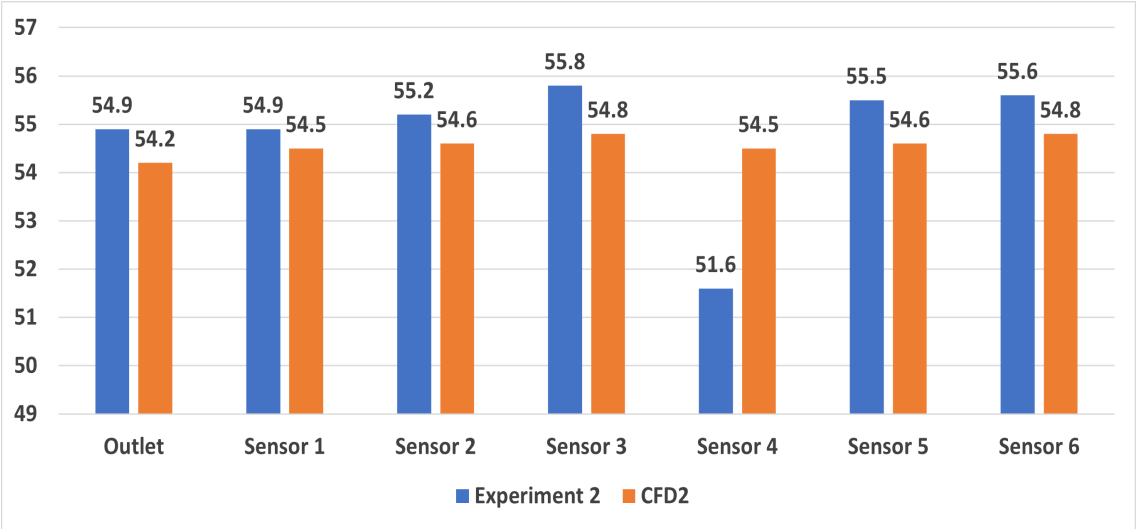

(b) Temperature of the thermocouples, from CFD and the first experiment for the bottom plate

Figure 4.4: Comparison of the data after refinement of the experiment and simulation, for the bottom plate

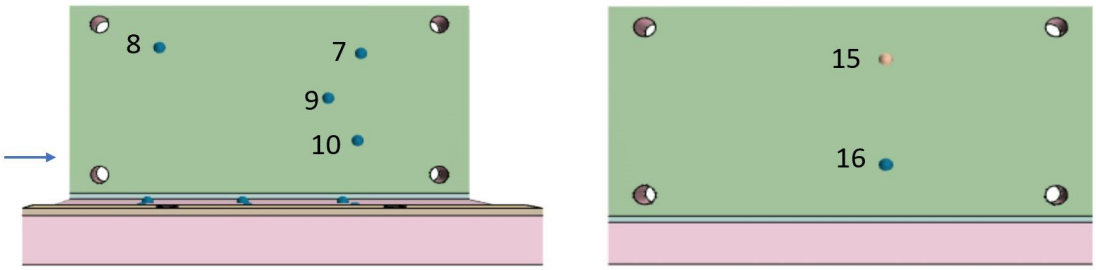

(a) Side view showing thermocouple positions on the back plate:
inner surface, outer surface (from left to right), with an arrow indicating the inlet hole

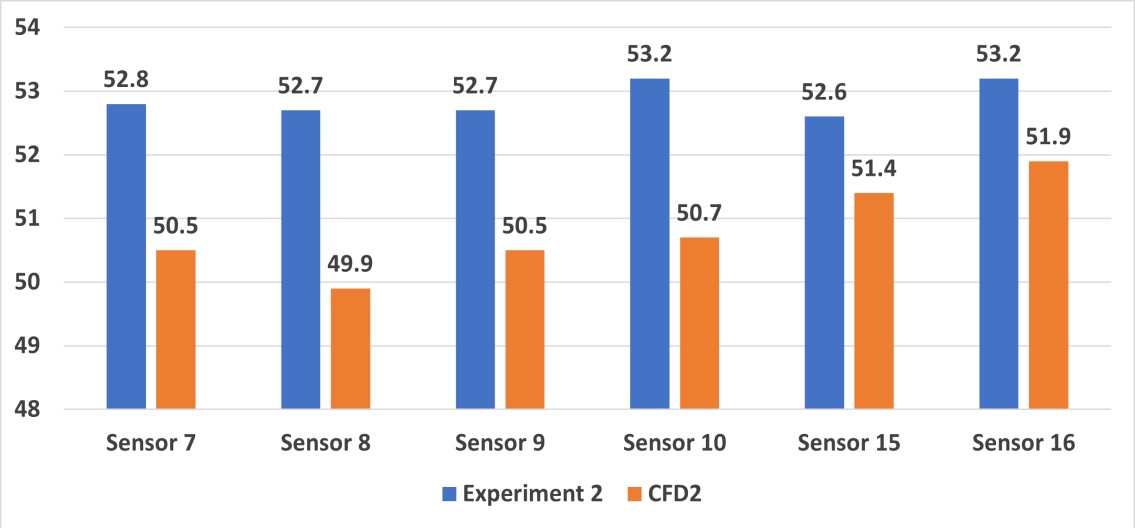

(b) Temperature of the thermocouples, from CFD and the first experiment for the back plate

Figure 4.5: Comparison of the data after refinement of the experiment and simulation, for the back plate

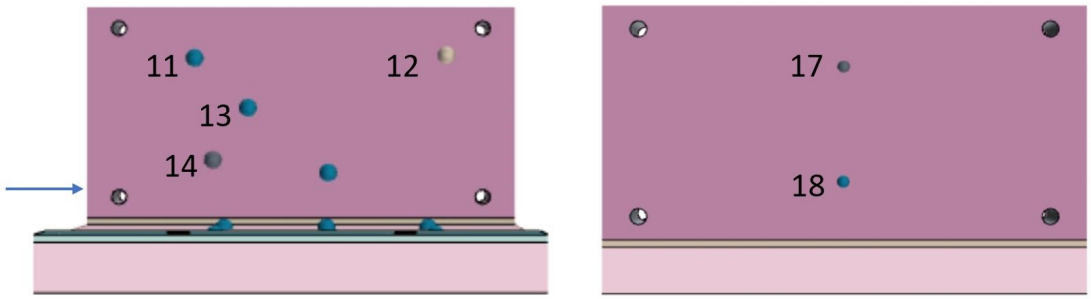

(a) Side view showing thermocouple positions on the front plate:
inner surface, outer surface (from left to right), with an arrow indicating the inlet hole

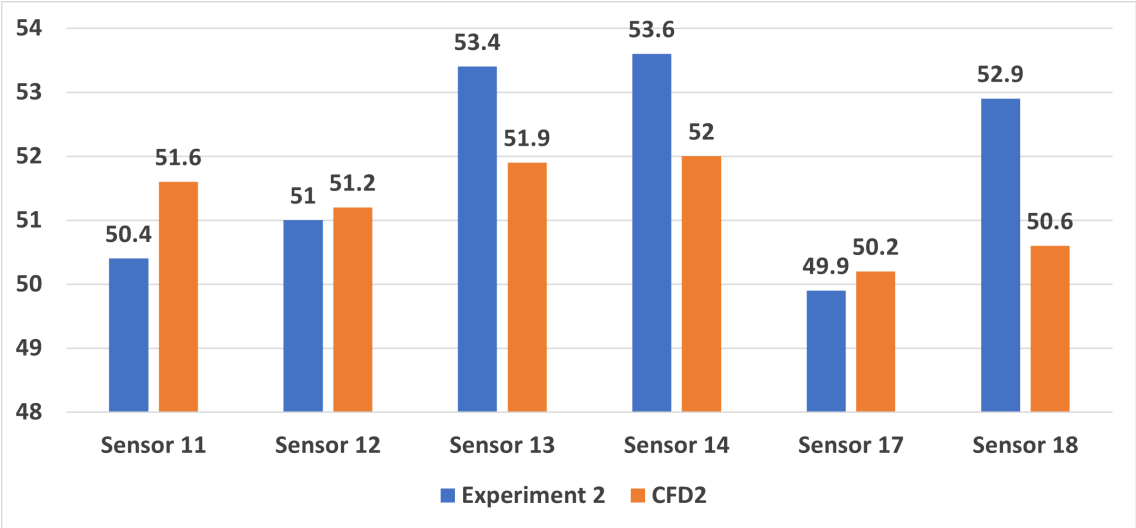

(b) Temperature of the thermocouples, from CFD and the first experiment for the front plate

Figure 4.6: Comparison of the data after refinement of the experiment and simulation, for the front plate

The analysis of Figures 4.4, 4.5, and 4.6 clearly demonstrates a significant reduction in deviations. The thermocouples exhibited values that were much closer to the realistic values obtained from the CFD simulations. This outcome highlights the beneficial impact of the adhesive tapes in terms of improving insulation and minimizing the influence of the surrounding air. Additionally, the utilization of a more realistic velocity and a properly dimensioned box that accurately represents the chamber contributed significantly to the development of a robust model at this stage.

The analysis of the figure 4.7 demonstrates the notable impact of incorporating various enhancements into the simulation. The improved simulation accurately represents the flow rate within the chamber, resulting in more precise predictions of the heat transfer coefficient pattern, particularly in scenarios involving forced convection. Notably, the airflow enters the chamber from the lower left region, as depicted

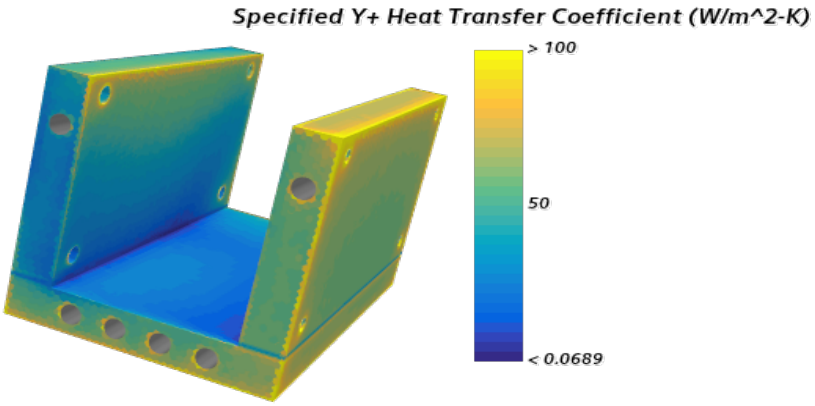

(a) Heat transfer coefficient distribution on jig's surface

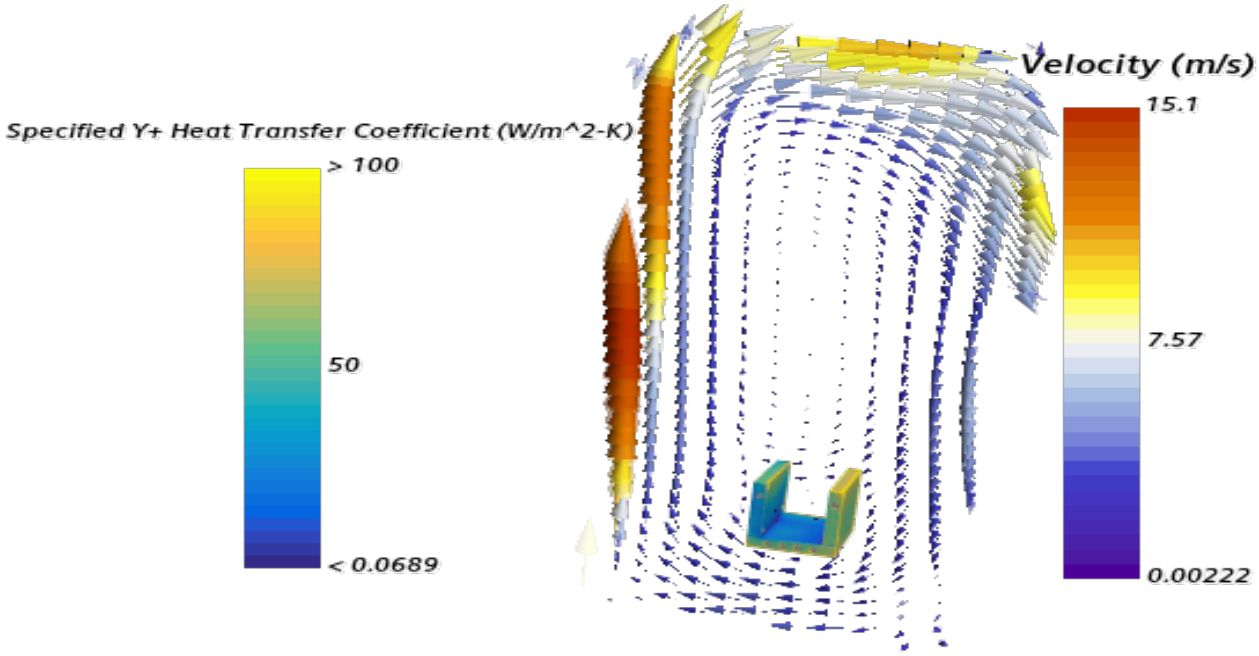

(b) Spatial distribution of velocity vectors within the chamber

Figure 4.7: Visualization of heat transfer coefficient and velocity distribution within the chamber using an empty jig

in 4.7, and undergoes recirculation within the chamber. Consequently, the airflow predominantly impinges on the front plate of the jig rather than the back plate. This preferential impingement enhances the heat transfer coefficient by facilitating efficient heat dissipation from the surface. Such enhancement arises from the increased convective heat transfer attributed to improved fluid mixing and heightened fluid motion. Furthermore, the diverse airflow directions that impact the empty jig's

plate promote convective heat transfer by fostering optimal interaction between the fluid and the surface, while concurrently reducing the thickness of the boundary layer.
As stated previously in Section 1.3, the uncertainties associated with the thermocouple data were within the range of ± 1, which indicated satisfactory results at this stage of the study. Consequently, the project progressed to its second phase, which involved the integration of the battery cell into the simulation.

4.3 The prismatic battery cell thermal model results

Having achieved a satisfactory alignment for the empty jig, indicating a reliable model that accurately represents the chamber, the next step involved incorporating the battery cell into the simulation domain. This allowed us to observe the distribution of heat generation from the battery cell onto the surface of the jig.

The battery cell was initially set at a state of charge (SOC) of 0.2 and a current of 0 A. Subsequently, the current rapidly increased to a high value. To visualize these changes over time, a normalized graph depicting the variations in SOC and current is provided below.

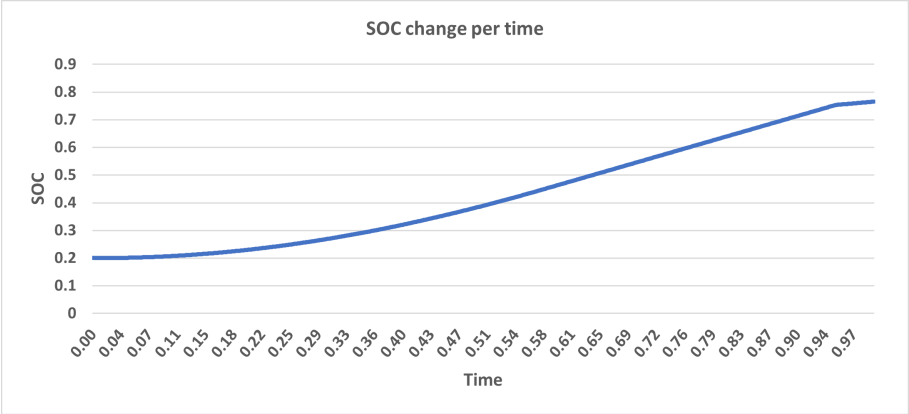

(a) SOC changes during the test time span

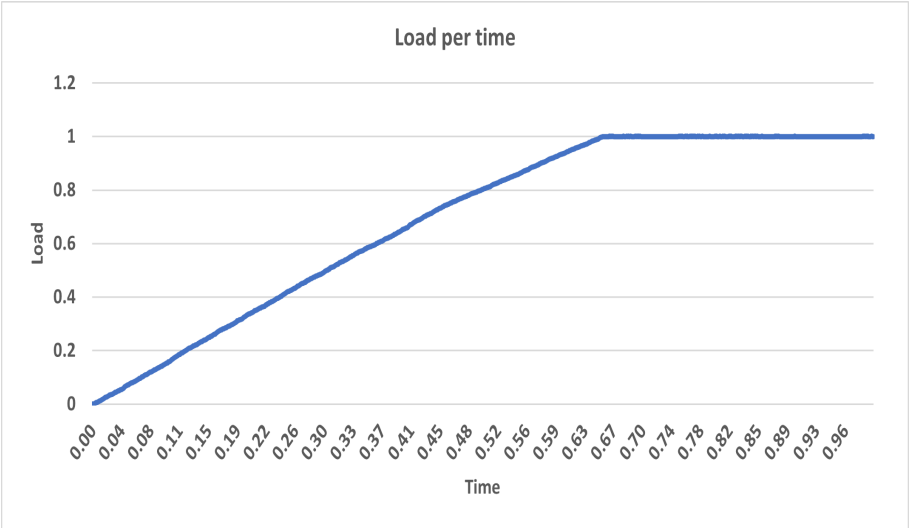

(b) Normalized load per time

Figure 4.8: The normalized state of charge (SOC) and load of the battery cell throughout the experimental test

This simulation provided invaluable data regarding the distribution of heat across different plates, as well as the transfer of heat to the surrounding air. Furthermore, it highlighted the impact of liquid cooling under the scenario where both the ambient temperature and coolant temperature were set at 35°C, as illustrated in the table below:

Object	Percentage of Heat Transfer Received
Air	3.3
Bottom Plate	48.8
Front Plate	23.7
Back Plate	24

Table 4.3: Comparison of heat transfer from the CAN of the cell to the jig and air

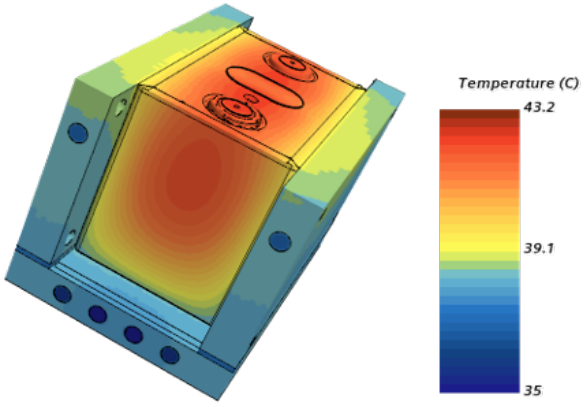

Figure 4.9: A representation of the simulation domain, depicting the temperature distribution of the battery cell at the end of the simulated time period

As depicted in Figure 4.9, a notable concentration of heat is observed on the upper surface of the battery cell's can. This phenomenon primarily arises from the heat generation by the tabs, alongside the battery cell, coupled with limited heat transfer to the surrounding airflow.

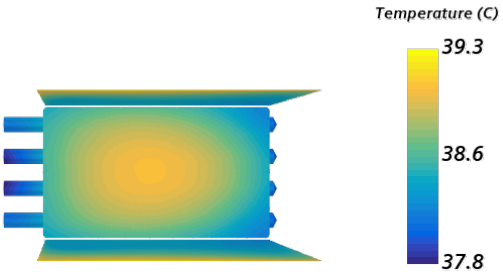

(a) Top-view temperature distribution of the battery cell's CAN

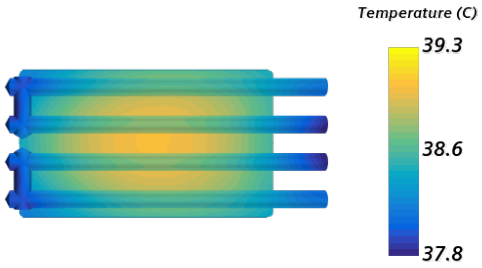

(b) Bottom-view temperature distribution of the battery cell's CAN

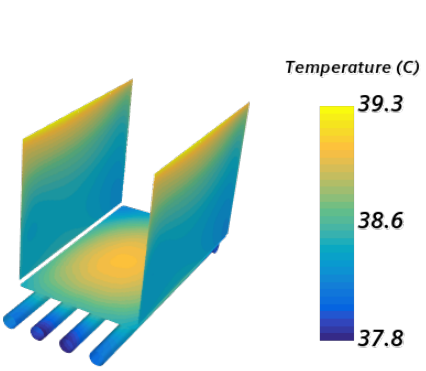

(c)

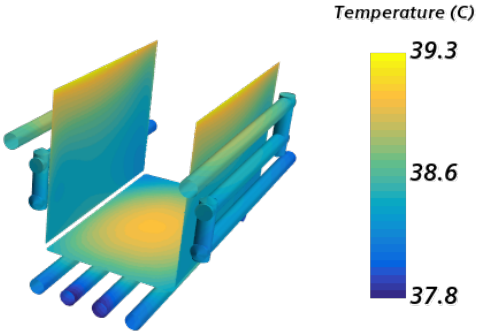

(d) Temperature distribution on for the coolant and the CAN's surface

Figure 4.10: Temperature distribution on the contacting sides of the CAN and the jig: an illustration

Figure 4.10 depicts the temperature distribution on the contacting sides of the battery cell's CAN with the jig. The top areas of the vertical sides of the CAN exhibit higher temperatures, indicating the presence of heat generated from the tabs and the battery cell itself. Additionally, upon comparing it with the vertical coolants in figure 4.10d, it is evident that as the coolant approaches the outlet points on the vertical plates, its temperature increases compared to the initial points on the bottom plate. This temperature increase is a result of earlier heat transfer within the bottom plate. Consequently, a lower temperature difference is observed between the coolant and the CAN of the cell, signifying reduced heat transfer since the driving force for heat transfer diminishes. Consequently, the top of the battery cell's CAN exhibits higher temperatures, as also shown in figure 4.9, particularly in the top areas of the vertical plates as well.

Another observation depicted in Figures 4.10a, 4.10b, and 4.11 regarding the bottom plate and the CAN's bottom surface is the presence of lower temperatures on the opposite side of the entry points, where the internal channels alter their directions

to guide the flow of coolant towards the outer regions. This alteration in flow direction led to the formation of distinct flow patterns and structures. Consequently, the boundary layer thickness and velocity profile of the coolant were affected. These modifications in the coolant's flow characteristics bring about changes in the convective heat transfer coefficient within the channels, resulting in an enhanced rate of heat transfer.

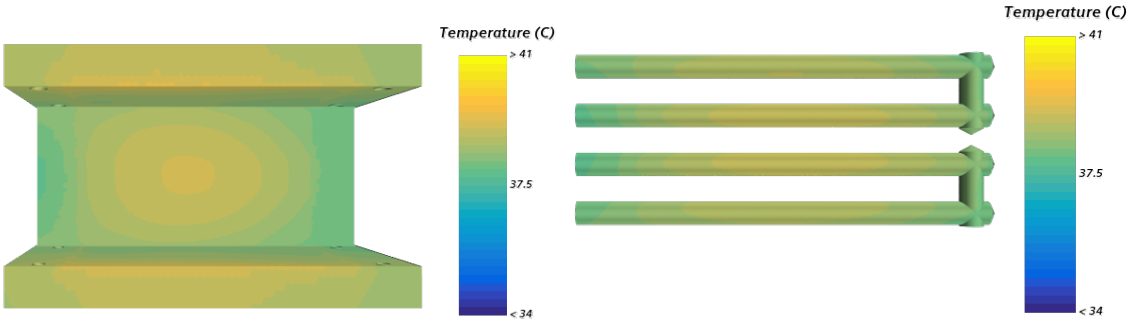

(a) Top-view temperature distribution of the bottom plate of the jig

(b) Top-view temperature distribution of the coolant's of the bottom plate

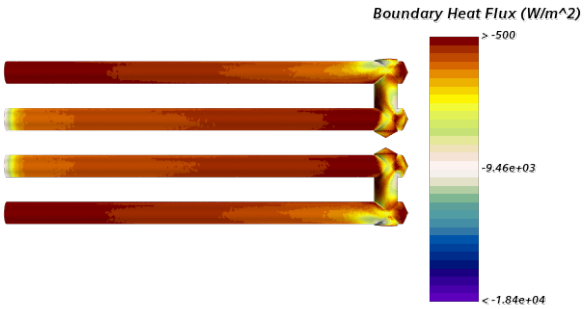

(c) Heat flux. from the bottom plate of the jig to the two internal channels

Figure 4.11: Temperature and heat flux for the bottom plate of the jig and its channels

5
Conclusion

The primary aim of this thesis was to develop and refine a comprehensive computational fluid dynamics (CFD) model from the ground up. The model's purpose was to analyze the thermal and air conditioning performance of a battery cell within a controlled test chamber, with a specific focus on evaluating the effectiveness of the existing jig design and also testing conditions. To ensure the model's reliability, rigorous comparisons were conducted between the CFD simulations and experimental data at various stages of the study.
Throughout the course of this study, careful consideration was given to numerous assumptions regarding the physical characteristics of the model and the behavior of the battery cell. The resulting findings are highly encouraging, as they provide valuable insights into the response of the jig to the heat generated by the battery cells. It was particularly observed that the bottom plate plays a significant role in absorbing heat, while the contribution from the surrounding air is minimal. These findings serve as a solid foundation for future advancements in fixture and experimental design, with the primary objective of preventing battery cell damage during testing through the implementation of more efficient heat absorption mechanisms. Furthermore, at the end of the project, it was noted that certain components surrounding the jig during the test not the simulation, such as the plastic cover and the tapes on top of the cell, as well as the thermal absorption pad between the jig and cell, contribute to the cancellation of a significant amount of heat generated by the battery cell. By removing these materials and implementing additional improvements while ensuring safety measures are upheld, a more effective heat transfer between the cell and the jig can be achieved. This, in turn, will facilitate more efficient climatization of the battery cell.

Although the current model demonstrates significant potential, there are still areas that require refinement to achieve a more accurate representation of the physical phenomena involved. These aspects will be discussed in detail in the chapter 6, highlighting avenues for further research and development.

6
Future work

Throughout this research, several assumptions were made, presenting potential avenues for future exploration and implementation. Firstly, it is strongly advised to conduct a thorough investigation into the exact material properties of the battery cell. This includes analyzing the necessity of the plastic cover on the surface of the CAN and the presence of a pressure absorption pad. As these materials and their properties were observed towards the end of the project, they were not incorporated into the simulation due to time constraints. Integrating these specific properties into the simulation would substantially enhance the accuracy of the model. Furthermore, it is advisable to perform a time step sensitivity study for this model in order to validate the current results. This analysis was not conducted within the scope of the project due to time limitations. By systematically varying the time step and examining its impact on the simulation outputs, the robustness and reliability of the results can be further confirmed.

Additionally, the utilization of entropy tables, aligned with the ECM table, can contribute to a more precise representation of the battery cell's thermal properties during charge and discharge cycles. Implementing these tables would result in a more accurate heat generation pattern and improve the overall fidelity of the simulation.

Regarding the experimental setup, the design was well-conceived, taking into account the capabilities of the battery lab and providing valuable data. However, for the possible further enhance of the measurement accuracy, it is suggested to install sensors within the jig in closer proximity to the battery cell. This can be achieved, for example, by introducing drilled holes strategically placed for sensor placement.

By addressing these aspects in future research, the understanding of battery cell behavior and the performance of the jig can be further refined, leading to more precise simulations and improved data acquisition methodologies.

Bibliography

[1] He, Fan, Li, Xuesong, and Ma, Lin. *Combined experimental and numerical study of thermal management of battery module consisting of multiple Li-ion cells. International Journal of Heat and Mass Transfer*, vol. 72, pp. 622–629, 2014. Elsevier.

[2] Versteeg, Henk Kaarle and Malalasekera, Weeratunge. *An introduction to computational fluid dynamics: the finite volume method*. Pearson education, 2007.

[3] Andersson, Bengt, et al. *Computational fluid dynamics for engineers*. Cambridge University Press, 2011.

[4] Energy Cascade of Turbulent Flows. Engineering Education System, 1993. Available at: `https://skill-lync.com/student-projects/week-5-turbulence-modelling-challenge-19`.

[5] Simcenter Star-CCM+ User Guide. Siemens Digital Industries Software, Year. Available at: `star/ccm/2206/STAR-CCM+2206/doc/en/online/index.html#page/connect%2Fsplash.html`.

[6] Bergman, Theodore L, Lavine, Adrienne S, Incropera, Frank P, and DeWitt, David P. *Incropera's principles of heat and mass transfer*. Wiley Global Education, 2017.

[7] Xie, Yongqi, Shi, Shang, Tang, Jincheng, Wu, Hongwei, and Yu, Jianzu. *Experimental and analytical study on heat generation characteristics of a lithium-ion power battery*. International Journal of Heat and Mass Transfer, 122:884–894, 2018. Elsevier.

[8] Liu, Kai, Yayuan Liu, Dingchang Lin, Allen Pei, and Yi Cui. *Materials for lithium-ion battery safety. Science advances* 4, no. 6 (2018): eaas9820.

[9] Barg-Becker, Christina and Domanski, Reinhold. *Adhesive Tapes and Structural Bonding—The Best of Both Worlds. adhesion ADHESIVES+ SEALANTS*, vol. 15, no. 4, pp. 16–19, 2018.

[10] Stylus 740 Double-Sided Tape, 24mm x 33m. Available at: `https://officenational.com.au/shop/en/commercial/stylus-740-double-sided-tape-24mm-x-33m-7011982`.

[11] Heat Transfer by Natural Convection: Nusselt Number Formula and Its Significance. CADSYS, 2022. Available at: `https://www.cadsys25.com/2022/02/heat-transfer-by-natural-convection-nusselt-number-formula-and-its-significance-html?utm_content=cmp-true`

[12] WEISS NA. LI-IO for Lithium-Ion Energy Storage. [Online]. Available: `https://weiss-na.com/product/li-io-for-lithium-ion-energy-storage/` (Accessed: Month Day, Year).

[13] Comte-Bellot, G. (1976). Hot-wire anemometry. *Annual Review of Fluid Mechanics*, 8(1), 209–231. Retrieved from https://www.annualreviews.org/doi/abs/10.1146/annurev.fl.08.010176.001233

[14] Omni Instruments. *ThermoAir 6/64 Hot Wire Anemometer with 0-1V or 4-20mA Output*. [Online]. Available: https://www.omniinstruments.co.uk/thermoair-6-64-hot-wire-anemometer-with-0-1v-or-4-20ma-output.html (accessed: May 2023).

[15] Tappeiner, Lukas, Marc Oldenburger, Benjamin Bedürftig, and Frank Woittennek. *A new approach to modeling and simulation of the nonlinear, fractional behavior of Li-ion battery cells*. Journal of Energy Storage, vol. 50, pp. 104106, 2022. Elsevier.

[16] A simple ECM of lithium-ion batteries. Available at: https://www.researchgate.net/figure/A-simple-ECM-of-lithium-ion-batteries_fig1_282476776.

[17] Elmahdi, Fadlaoui, Lagrat Ismail, and Masaif Noureddine. *Fitting the OCV-SOC relationship of a lithium-ion battery using genetic algorithm method*. In E3S Web of Conferences, vol. 234, p. 00097, 2021. EDP Sciences.

[18] Testbook.com. Internal Resistance of a Cell. Available online: https://testbook.com/physics/internal-resistance-of-a-cell (Accessed on [insert date accessed]).

[19] "Polarization Resistance." Corrosionpedia. Accessed May 2023. Available at: https://www.corrosionpedia.com/definition/899/polarization-resistance

[20] Electronics Tutorials. *Time Constant in RC Circuit*. Available online: https://www.electronics-tutorials.ws/rc/time-constant.html (accessed on May 22, 2023).

A

Some figures and graphs

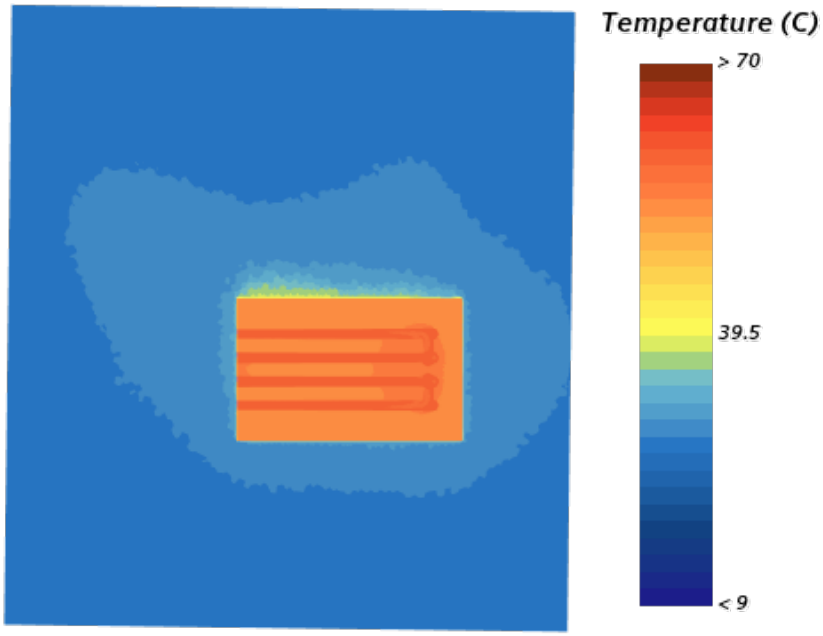

Figure A.1: Temperature distribution on jig's bottom plate post-improvements in measurements and simulations

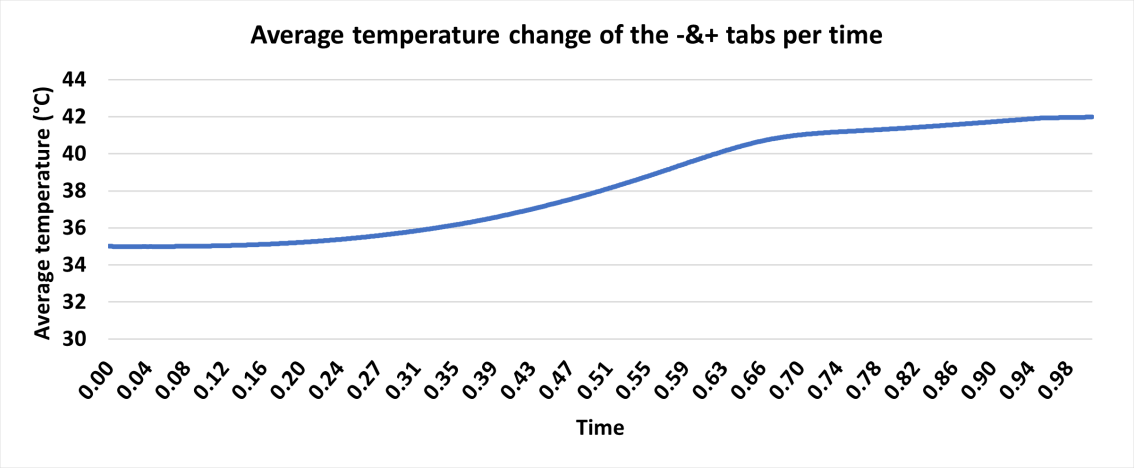

Figure A.2: Average temperature change of the negative and positive tabs of the cell per time

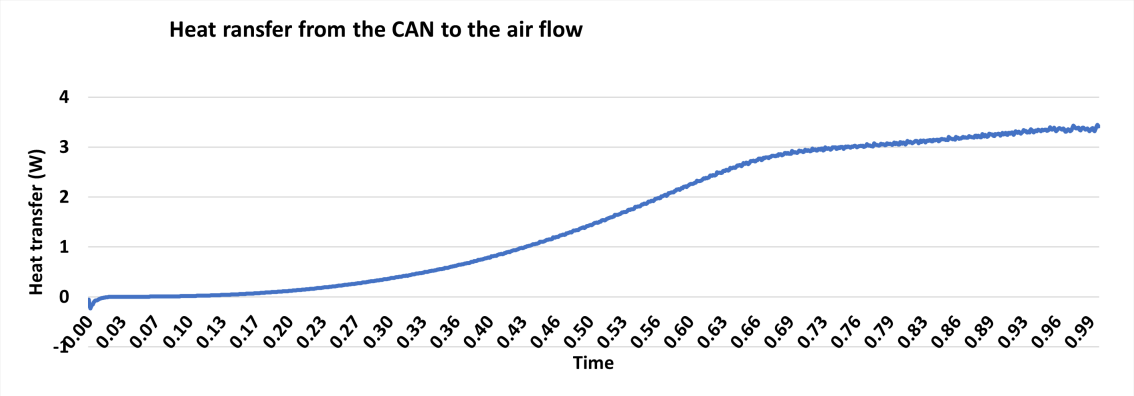

Figure A.3: Heat transfer from the CAN of the cell to the air flow of the chamber per time

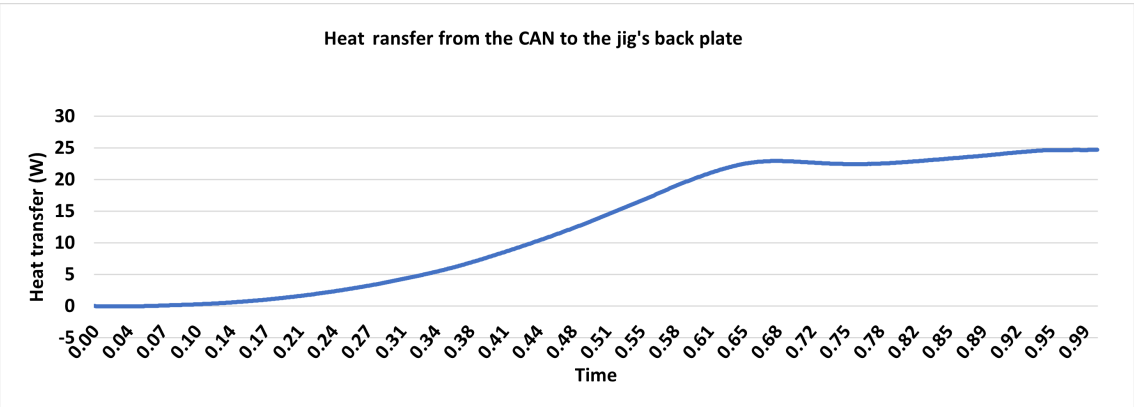

Figure A.4: Heat transfer from the CAN of the cell to the back plate of the jig per time

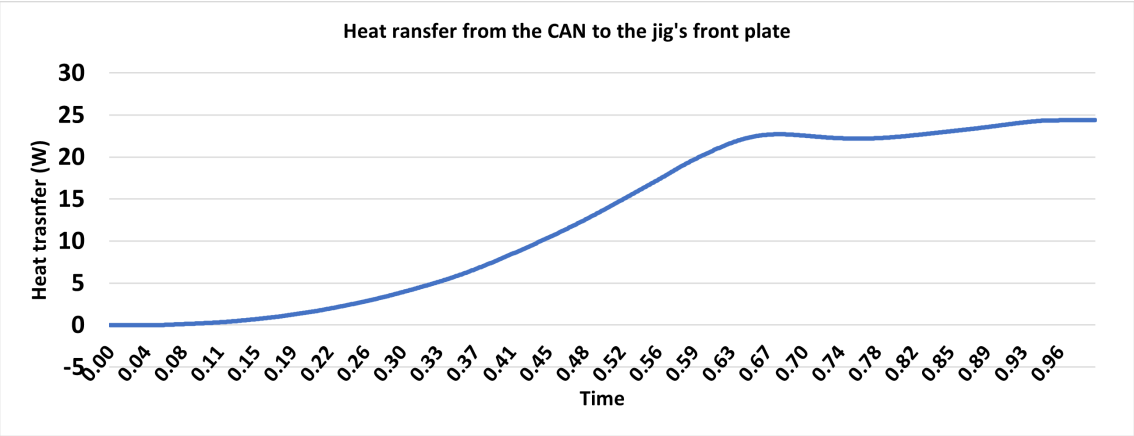

Figure A.5: Heat transfer from the CAN of the cell to the front plate of the jig per time

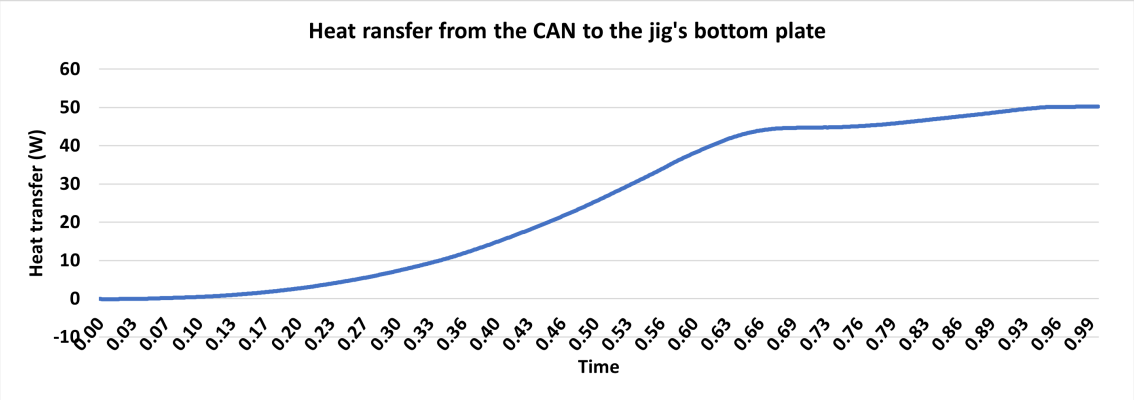

Figure A.6: Heat transfer from the CAN of the cell to the bottom plate of the jig per time

DEPARTMENT OF MECHANICS AND MARITIME SCIENCES
CHALMERS UNIVERSITY OF TECHNOLOGY
Gothenburg, Sweden
www.chalmers.se

CHALMERS
UNIVERSITY OF TECHNOLOGY